Inorganic Chemistry
Article
pubs.acs.org/IC

A Combined Experimental and DFT/TD-DFT Investigation of Structural, Electronic, and Cation-Induced Switching of Photophysical Properties of Bimetallic Ru(II) and Os(II) Complexes Derived from Imidazole-4,5-Dicarboxylic Acid and 2,2′-Bipyridine

Shyamal Das, Srikanta Karmakar, Debasish Saha, and Sujoy Baitalik*

Department of Chemistry, Inorganic Chemistry Section, Jadavpur University, Kolkata - 700 032, India

Supporting Information

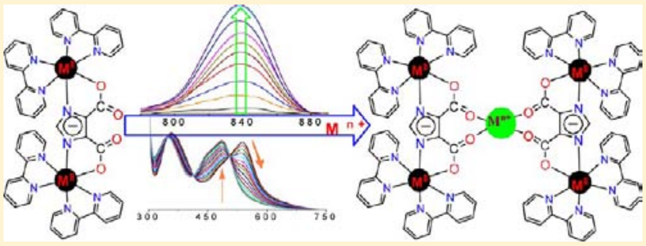

ABSTRACT: Experimental results coupled with computational studies were utilized to investigate the structural and electronic properties of mixed-ligand bimetallic ruthenium(II) and osmium(II) complexes of composition $[(bpy)_2M(Imdc)M(bpy)_2]^+$ [M = Ru^{II} (**1**) and M = Os^{II} (**2**)], where H_3Imdc = imidazole-4,5-dicarboxylic acid and bpy = 2,2′-bipyridine. The X-ray crystal structures of both the bimetallic complexes were determined which showed that compound **1** crystallizes in monoclinic form with space group *P*2(1)/*c*, while **2** is obtained in orthorhombic form with the space group *Pca*2(1). The optimized geometrical parameters for the complexes computed both in the gas phase and in solution are reported and compared with the single-crystal X-ray data. The absorption spectra, redox behaviors, and luminescence properties of the complexes were thoroughly investigated. The complexes display very intense, ligand-centered absorption bands in the UV and moderately intense MLCT bands in the visible regions. While the Ru(II) complex displays moderately strong luminescence, the corresponding Os(II) complex does not luminesce at room temperature. Both the bimetallic complexes show two successive one-electron reversible metal-centered oxidations. The effect of alkali, alkaline earth, and transition metal cations on the absorption and emission spectral behavior of the complexes has also been studied in detail. As compared to the luminescence intensities and the quantum yields of the free complexes, those of the complexes were enhanced substantially in the presence of selective cations showing cation-induced molecular switching behaviors. Density functional theory (DFT) and time-dependent DFT (TD-DFT) studies provide insight into the nature of the ground and excited states with resulting detailed assignments of the orbitals involved in absorption and emission transitions. In particular, the blue-shifts of the absorption and emission bands in the presence of cations are also reproduced by our calculations.

INTRODUCTION

Polypyridine complexes of d^6 transition-metals such as ruthenium(II) and osmium(II) are currently among the most studied compounds in coordination chemistry because of their unique combination of photophysical, photochemical, and electrochemical properties such as low-lying metal-to-ligand charge transfer (MLCT) excited states, intense luminescence in the visible region of the spectrum, relatively long radiative lifetimes, and thermal and photochemical stabilities.[1] These properties often can be tuned by ramification of ligand structures and by introducing coligands in complexes.[1] Consequently, polypyridyl complexes of these metals are potentially useful in many important areas of research such as photochemical conversion of solar energy, molecular electronic devices, and molecular sensors and switches.[1,2] In this context, it is worth mentioning that molecules which could absorb and emit light in the near-infrared (NIR) regions (700−1000 nm) are of particular interest because NIR dyes are important for biological imaging as they exhibit low light scattering and deep penetration behaviors.[3] More importantly, most biological samples absorb weakly in the long-wavelength region, thus decreasing the background absorbance and autofluorescence.[3] A number of ruthenium(II) and osmium(II) polypyridine-based compounds emitting in the NIR region have been designed,[1,4,5] although such reports are relatively few and some of them suffer from low emission quantum yields, short excited-state lifetimes, and a lack of photochemical stabilities. Hence, new NIR-emitting dyes with improved photophysical properties are still in demand. In particular, di- and polynuclear metal complexes in which mononuclear polypyridyl units are connected by conjugated bis-bidentate bridging ligands have received special attention since they provide an important basis for understanding electronic interactions between the metal centers and photoinduced intramolecular electron and energy transfer processes. The extent of electronic communication between the metal centers in such complexes, mediated through the intervening bridging ligands, strongly influences their ground- and excited-state properties and redox activities.[1,5] The role of a bridging ligand in this context is determined by several factors such as the

Received: November 23, 2012
Published: June 5, 2013

arrangement and σ/π donor/acceptor properties of the coordination sites, the length and rigidity of spacers, the access of pathways for electron delocalization, and the charge of the ligand. If a bridging ligand can respond to an external perturbation (light, anion, cation, pH, etc.), sensing or switching of properties in a complex species may take place.[6−10] Indeed, depending upon the extent of perturbation of these properties, stimuli-driven molecular switches can be developed.[6−10]

There is currently a considerable effort devoted for the synthesis of metalloreceptors for recognizing and signaling the presence of substrates, such as neutral molecules or ions due to the diversity of their geometry, redox activity, and rich photophysical properties.[6−12] Such molecular sensors are usually constructed by combining a complexation pocket, designed for the specific binding of an incoming substrate, with a reporter unit for modulating a signal, usually color, luminescence, or electrochemical potentials, as a result of host−guest interaction.[10−13] In our search for an appropriate system for the construction of cation-driven molecular switches, we have synthesized and structurally characterized bimetallic Ru(II) and Os(II) complexes of the type $[(bpy)_2M(Imdc)M(bpy)_2]^+$ ($M = Ru^{II}$ and Os^{II}), where H_3Imdc = imidazole-4,5-dicarboxylic acid and bpy = 2,2′-bipyridine exhibit both chromophoric properties and cation-binding abilities. As seen in Chart 1, two free >C═O groups in the already coordinatively saturated metal complexes adopt a *cis* arrangement, and this pair of externally directed O atoms of the coordinated imidazole-dicarboxylate ($Imdc^{3-}$) moiety could be used as the trap for cations in solution. We recently reported the synthesis, characterization, and pH-induced tuning of photophysical and redox properties of monometallic ruthenium(II) and osmium(II) mixed chelates of composition $[(bpy)_2M^{II}(H_2Imdc)]^+$ through experimental and theoretical investigations.[14] It may be mentioned that, since the first report of the syntheses of the imidazole-bridged bimetallic complexes of various 3d transition metal ions by Costes and collaborators,[15] a lot of substituted imidazoles and imidazoles in combination with other N-heterocyclic rings have been employed for the syntheses of homo- and heterobimetallic complexes of various transition metals including those of Ru(II) and Os(II).[16,17] Moreover, multifunctional N-heterocyclic carboxylates, such as imidazole- and pyrazole-dicarboxylic acids, owing to the presence of multioxygen and nitrogen atoms can coordinate with various metal ions in versatile ways, resulting in the formation of various metal−organic frameworks (MOFs) with specific topologies and useful properties. Designing of novel MOFs is one of the most challenging fields because of the important role played by them in the areas of catalysis, sorption, sensors, nonlinear optics, magnetism, and so on.[18] We report herein the synthesis, structural characterization, electrochemical behavior, and photophysical properties of the bimetallic Ru(II) and Os(II) complexes of composition $[(bpy)_2M(Imdc)M(bpy)_2]^+$ and their interactions with a series of metal ions in solution. The emission of these complexes falls in the near-IR region, an occurrence still uncommon for most of the ruthenium(II) polypyridine complexes.[4,5] As will be seen, the luminescence activities of the complexes are switched on by the presence of selective metal ions such as alkali, alkaline earth, and d^{10} transition metals such as Zn(II), Cd(II), and Hg(II). In this contribution, we will also carry out density functional theory (DFT) and time-dependent DFT (TD-DFT) calculations of the complexes in both singlet and triplet excited states to gain a better understanding of the electronic structure and excited-state properties of the complexes. As will be seen, with a reasonable computational effort TD-DFT well reproduces the experimentally observed spectroscopic properties of the complexes.

Chart 1

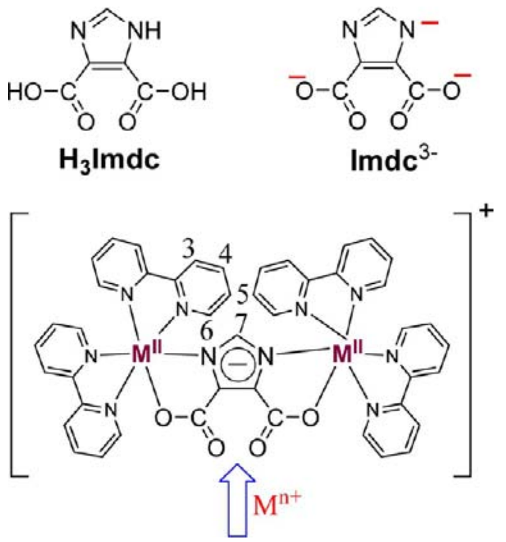

EXPERIMENTAL SECTION

Materials. Reagent grade chemicals obtained from commercial sources were used as received. Solvents were purified and dried according to standard methods. 4,5-Imidazole dicarboxylic acid was purchased from Sigma-Aldrich. *cis*-$[Ru(bpy)_2Cl_2]\cdot 2H_2O$[19] and *cis*-$[Os(bpy)_2Cl_2]$[20] were prepared by the literature method. $AgClO_4$ was prepared from silver carbonate and perchloric acid and recrystallized from benzene.

Caution! $AgClO_4$and perchlorate salts of the metal complexes used in this study are potentially explosive and therefore should be handled with care in small quantities.

Preparation of $[(bpy)_2Ru(Imdc)Ru(bpy)_2](ClO_4)$ (1). To a stirred suspension of *cis*-$[Ru(bpy)_2Cl_2]\cdot 2H_2O$ (0.26 g, 0.5 mmol) in ethanol (50 mL) under nitrogen protection was added solid $AgClO_4$ (0.22 g, 1.0 mmol). After 0.5 h, the precipitated AgCl was removed by filtration, and the filtrate containing $[Ru(bpy)_2(EtOH)_2]^{2+}$ was treated with powdered H_3Imdc (0.04 g, 0.25 mmol) and triethylamine (0.08 g, 0.75 mmol) and refluxed for 8 h. The solution was filtered hot and concentrated to approximately 10 mL, which deposited the red orange compound on cooling in an ice bath. After 2 h, the product was collected by filtration and recrystallized twice from methanol (159 mg, yield: 58%). Calcd for $C_{45}H_{33}N_{10}ClO_8Ru_2$: C, 50.03; H, 3.06; N, 12.97. Found: C, 50.01; H, 3.05; N, 12.98. ^1H NMR data {300 MHz, DMSO-d_6, δ/ppm, see Chart 1 for atom numbering}: 8.89 (d, 2H, J = 5.5 Hz, H6), 8.68 (d, 4H, J = 8.2 Hz, H3), 8.62 (d, 2H, J = 8.2 Hz, H3), 8.48 (d, 2H, J = 8.1 Hz, H3), 8.20 (t, 2H, J = 7.8 Hz, H4), 8.00 (t, 2H, J = 7.8 Hz, H4), 7.91−7.84 (m, 4H, H5), 7.71 (t, 2H, J = 7.8 Hz, H4), 7.58 (d, 2H, J = 5.5 Hz, H6), 7.54 (d, 2H, J = 5.6 Hz, H6), 7.31−7.21 (m, 4H, H4 + H5), 7.09−7.05 (m, 4H, H5 + H6), 5.26 (s, 1H, H7). ESI-MS (positive, CH_3CN): m/z = 490.59 (100%) $[(bpy)_2Ru(HImdc)Ru(bpy)_2]^{2+}$, m/z = 501.07 (73%) $[(bpy)_2Ru(Imdc)\ Ru(bpy)_2(Na)]^{2+}$. UV−vis [$CH_3CN$; λ_{max}/nm (ε/M^{-1} cm^{-1})]: 538 (14700), 480 sh (9380), 358 (16740), 295 (75300), 247 (40940).

$[(bpy)_2Os(Imdc)Os(bpy)_2](ClO_4)\cdot 2H_2O$ (2). A mixture of *cis*-$[Os(bpy)_2Cl_2]$ (0.29 g, 0.5 mmol), H_3Imdc (0.039 g, 0.25 mmol), and triethylamine (0.08 g, 0.75 mmol) in 80 mL of 1:1 (v/v) ethanol−water was heated under reflux for 60 h with continuous stirring. The solution was filtered and cooled in an ice bath, and an aqueous solution (5 mL) of $NaClO_4$ (1 g) was added to precipitate the complex as its perchlorate salt. The dark, shining microcrystals that deposited were collected by filtration after 3 h. The product was recrystallized twice from methanol; yield 0.18 g (56%). Calcd for $C_{45}H_{37}N_{10}ClO_{10}Os_2$: C, 41.78; H, 2.88; N, 10.83 Found: C, 41.75; H, 2.90; N, 10.80. ^{1}H NMR data {300 MHz, DMSO-d_6, δ/ppm, see Chart 1 for atom numbering}: 8.70−8.65 (m, 6H, H3+H6), 8.55 (d, 2H, J = 8.2 Hz, H3), 8.39 (d, 2H, J = 8.2 Hz, H3), 7.85 (t, 2H, J = 7.8 Hz, H4), 7.72 (t, 2H, J = 6.5 Hz, H4), 7.61 (t, 4H, J = 6.7 Hz, H5), 7.46 (d, 2H J = 5.8 Hz, H6), 7.40−7.35 (m, 4H, H4 + H6), 7.13−7.04 (m, 4H, H4 + H5), 6.94 (d, 2H, J = 5.5 Hz, H6), 6.82 (t, 2H, J = 6.6 Hz, H5), 5.06 (s, 1H, H7). ESI-MS (positive, CH3CN): m/z = 579.56 (48%) $[(bpy)_2Os(HImdc)Os(bpy)_2]^{2+}$, m/z = 590.55 (100%) $[(bpy)_2Os(Imdc)Os(bpy)_2(Na)]^{2+}$. UV−vis [$CH_3CN$; λ_{max}/nm (ε/M^{-1} cm^{-1})]: 805 (br) (3800), 710 (br) (4700), 544 (15460), 438 (sh) (15600), 362 (19100), 295 (82380), 244 (47600).

Physical Measurements. Elemental (C, H, and N) analyses were performed on a Perkin-Elmer 2400II analyzer. Electrospray ionization mass spectra (ESI-MS) were obtained on a Micromass Qtof YA 263 mass spectrometer. ^{1}H NMR and {^{1}H−^{1}H} COSY spectra were obtained on a Bruker Avance DPX 300 spectrometer using DMSO-d_6 solutions. Electronic absorption spectra were obtained with a Shimadzu UV 1800 spectrophotometer at room temperature. The binding studies of the receptor with different cations were carried out in acetonitrile solution. For a typical titration experiment, 2 μL aliquots of a given cation (2.5×10^{-3} M) were added to a 2.5 mL solution of the complex (1.5×10^{-5} M in acetonitrile). Hydrated perchlorate salts of the metals were used for titration experiments.

Steady-state emission spectra were recorded on a Perkin-Elmer LS55 fluorescence spectrophotometer. The room temperature spectra were obtained in acetonitrile, while the spectra at 77 K were recorded in 4:1 ethanol−methanol glass. Photoluminescence titrations were carried out with the same sets of solutions that were made for spectrophotometry. Quantum yields were determined by a relative method using $[Ru(bpy)_3]^{2+}$ as the standard. Time-correlated single-photon-counting (TCSPC) measurements were carried out for the luminescence decay of complexes. For TCSPC measurement, the photoexcitation was made at 450 nm using a picosecond diode laser (IBH Nanoled-07) in an IBH Fluorocube apparatus. The lifetimes of the Ru(II) complex were also recorded as functions of different cations. The fluorescence decay data were collected on a Hamamatsu MCP photomultiplier (R3809) and were analyzed by using IBH DAS6 software.

The electrochemical measurements were carried out with a BAS Epsilon electrochemistry system. A three-electrode assembly comprising a Pt (for oxidation) or glassy carbon (for reduction)-working electrode, Pt auxiliary electrode, and Ag/AgCl reference electrode were used. The cyclic (CV) and square wave voltammetric (SWV) measurements were carried out at 25 °C in acetonitrile solution of the complex (∼1 mM) and the concentration of the supporting electrolyte tetraethylammonium perchlorate (TEAP) was maintained at 0.1 M. All of the potentials reported in this study were referenced against the Ag/AgCl electrode, which under the given experimental conditions gave a value of 0.36 V for the ferrocene/ferrocenium couple.

Experimental uncertainties were as follows: absorption maxima, ±2 nm; molar absorption coefficients, 10%; emission maxima, ±5 nm; excited−state lifetimes, 10%; luminescence quantum yields, 20%; redox potentials, ±10 mV.

X-ray Crystal Structure Determination. Single crystals of both compounds were obtained by diffusing diethyl ether over the acetonitrile−methanol (1:2 v/v) solution of each. X-ray diffraction data for the crystals mounted on a glass fiber and coated with perfluoropolyether oil were collected on a Bruker-AXS SMART APEX II diffractometer at 296 K equipped with CCD detector using graphite monochromated Mo Kα radiation (λ = 0.71073 Å). Crystallographic data and details of structure determination are summarized in Table 1. The data were processed with SAINT, and absorption corrections were made with SADABS.[21] The structures were solved by direct and Fourier methods and refined by full-matrix least-squares based on F^2 using the WINGX software which utilizes SHELX-97.[22] For the structure solution and refinement the SHELXTL software package[23] was used. The nonhydrogen atoms were refined anisotropically, while the hydrogen atoms were placed with fixed thermal parameters at idealized positions. It may be mentioned that C29, C68, and C69 atoms of **1** and N1, C12, C31, C32, C35, C63, C68, and C83 atoms for **2** were refined isotropically. The electron density map also showed the presence of some unassignable peaks, which were removed by running the program SQUEEZE.[24]

Table 1. Crystallographic Data for $[(bpy)_2Ru(Imdc)Ru(bpy)_2](ClO_4)$ (1) and $[(bpy)_2Os(Imdc)Os(bpy)_2](ClO_4)\cdot 2H_2O$ (2)

	1	**2**
formula	$C_{45}H_{33}N_{10}ClO_8Ru_2$	$C_{45}H_{37}N_{10}ClO_{10}Os_2$
fw	1079.40	1289.66[c]
T (K)	293(2)	273(2)
cryst syst	monoclinic	orthorhombic
space group	$P2(1)/c$	$Pca2(1)$
a (Å)	26.0427(15)	28.7509(9)
b (Å)	13.4288(8)	14.9598(5)
c (Å)	28.7491(16)	24.9847(8)
α (deg)	90.00	90.00
β (deg)	104.579(2)	90.00
γ (deg)	90.00	90.00
V (Å^3)	9730.5(10)	10746.1(6)
D_c(g cm^{-3})	1.474	1.594
Z	8	8
μ (mm^{-1})	0.736	4.834
F(000)	4336	4976.0
θ range (deg)	2.20−24.44	2.16−25.17
data/restraints/params	16033/0/1169	18739/4/1185
GOF on F^2	1.184	0.827
R1[a] [$I > 2\sigma(I)$], wR2[b] (all data)	0.1182, 0.2425	0.0540, 0.1625
$\Delta\rho_{max}/\Delta\rho_{min}$ (e Å)	3.778 /−1.829	3.193/−1.245

[a] $R1(F) = [\sum \| F_o | - |F_c \| / \sum | F_o]$. [b] $wR2(F^2) = [\sum w(F_o^2 - F_c^2)^2 / \sum w(F_o^2)^2]^{1/2}$. [c] Four hydrogen atoms of two water molecules are omitted as shown in CIF of **2**.

CCDC reference numbers are 911717 for **1** and 911718 for **2**

Computational Methods. All calculations were performed with the Gaussian 09 program[25] package employing the DFT method with restricted Becke's three-parameter hybrid functional and Lee−Yang−Parr's gradient corrected correlation functional (R)B3LYP level of theory.[26−28] For all the elements 6-31G(d) basis set were used except ruthenium and osmium. The SDD basis set with effective core potential was employed for the ruthenium and osmium atoms.[29] On the other hand, the geometries of the Li-coordinated pentameric adducts abbreviated as [**1·Li·1**] and [**2·Li·2**] (Chart 2) were optimized in acetonitrile solution using (R)B3LYP/Lanl2DZ to get better results. To compute the UV−vis transitions of the compounds, the singlet excited-state geometries corresponding to the vertical excitations were optimized using the time-dependent DFT (TD-DFT) scheme starting with the ground-state geometries.[30−36] The excitation energies for **1** and **2**, protonated complexes of **1** and **2** abbreviated as [**1·H**] and [**2·H**], Li-coordinated trimetallic adduct of **1** abbreviated as [**1·Li**] (Chart 2) were computed within the acetonitrile solvent simulated by the conductor-like polarizable continuum (CPCM) model, whereas polarizable continuum model (PCM) were used for [**1·Li·1**] and [**2·Li·2**].[37−40] Only singlet−singlet transitions, that is, the spin-allowed transitions, have been taken into account. The percentage of contributions for vertical excitations were calculated by using Gauss sum 2.1.[41] The geometries of the lowest-energy triplet states of the complexes were also optimized in acetonitrile by using the TD-DFT method and employing the above models (CPCM and PCM). The local minimum on each potential energy surface was confirmed by frequency analysis. Orbital analysis was completed with GaussView.[42] In addition to TD-DFT, unrestricted Kohn−Sham (UKS) calculations were also performed directly on the triplet states of the complexes to calculate singlet−triplet energy gaps.

Chart 2

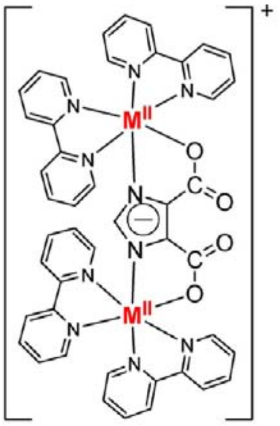

$\mathrm{M^{II} = Ru^{II}}$; 1
$\mathrm{M^{II} = Os^{II}}$; 2

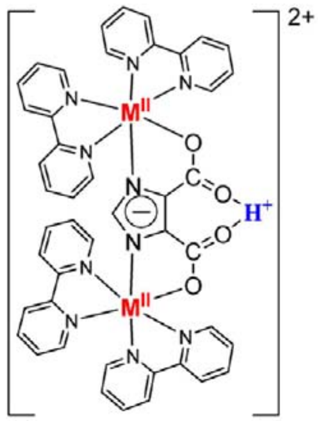

$\mathrm{M^{II} = Ru^{II}}$; [1.H]
$\mathrm{M^{II} = Os^{II}}$; [2.H]

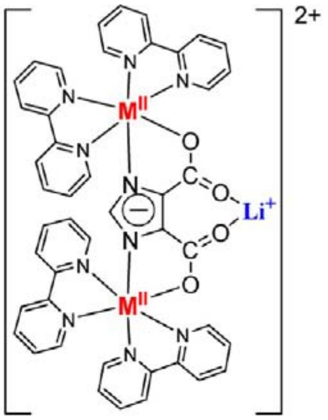

$\mathrm{M^{II} = Ru^{II}}$; [1.Li]
$\mathrm{M^{II} = Os^{II}}$; [2.Li]

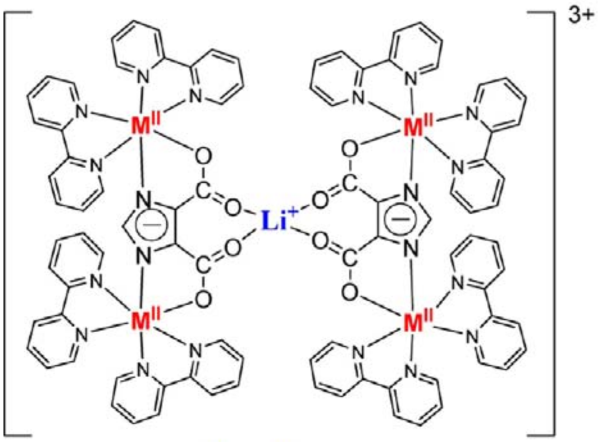

$\mathrm{M^{II} = Ru^{II}}$; [1.Li.1]
$\mathrm{M^{II} = Os^{II}}$; [2.Li.2]

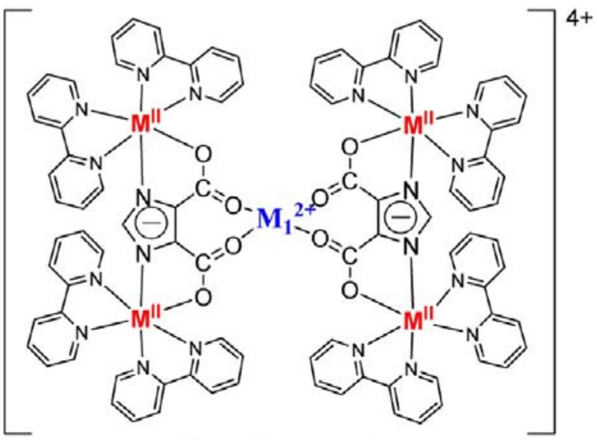

$\mathrm{M^{II} = Ru^{II}}$; [1.M$_1$.1]
$\mathrm{M^{II} = Os^{II}}$; [2.M$_1$.2]

$\mathrm{M_1^{2+}}$ = $\mathrm{Be^{2+}}$, $\mathrm{Mg^{2+}}$, $\mathrm{Ca^{2+}}$,
$\mathrm{Zn^{2+}}$, $\mathrm{Cd^{2+}}$, $\mathrm{Hg^{2+}}$,
$\mathrm{Mn^{2+}}$, $\mathrm{Fe^{2+}}$, $\mathrm{Co^{2+}}$, $\mathrm{Ni^{2+}}$, $\mathrm{Cu^{2+}}$

RESULTS AND DISCUSSION

Synthesis and Characterization. We have reported earlier that in terms of reaction rate and yield the solvated cation $[\mathrm{Ru(bpy)_2(EtOH)_2}]^{2+}$, generated by treating stoichiometric amounts of *cis*-$[\mathrm{Ru(bpy)_2Cl_2}]$ and $\mathrm{AgClO_4}$ in ethanol, acts as a better precursor relative to *cis*-$[\mathrm{Ru(bpy)_2Cl_2}]$ itself.[10,14] Thus, the bimetallic ruthenium(II) complex $[\mathrm{(bpy)_2Ru(Imdc)Ru(bpy)_2}](\mathrm{ClO_4})$ (**1**) was readily obtained by reacting 2 equiv of $[\mathrm{Ru(bpy)_2(EtOH)_2}]^{2+}$, 1 equiv of $\mathrm{H_3Imdc}$, and 3 equiv of triethylamine to deprotonate one imidazole NH and two carboxylic acid protons of imidazole-4,5-dicarboxylic acid. By contrast, the formation of $[\mathrm{(bpy)_2Os(Imdc)Os(bpy)_2}](\mathrm{ClO_4})$ (**2**) from *cis*-$[\mathrm{Os(bpy)_2Cl_2}]$ is very slow and requires a long reaction time (~60 h) and high boiling solvents like ethanol−water (1:1 v/v) mixture. Both the compounds were characterized by their elemental (C, H, and N) analyses, ESI mass, UV−vis, and ^{1}H NMR spectroscopic measurements, and the results are given in the Experimental Section. The ESI mass spectra of both the compounds in $\mathrm{CH_3CN}$ and their simulated isotopic distribution patterns are shown in Figures S1 and S2 (SI).

Description of the Crystal Structures of $[\mathrm{(bpy)_2Ru(Imdc)Ru(bpy)_2}](\mathrm{ClO_4})$ (1) and $[\mathrm{(bpy)_2Os(Imdc)Os(bpy)_2}](\mathrm{ClO_4})\cdot 2\mathrm{H_2O}$ (*2*). Complex **1** crystallized in monoclinic form with the space group *P*2(1)/*c*, while **2** is in orthorhombic form with the space group *Pca*2(1). ORTEP[43] representations of the cations in **1** and **2** along with the atom labels are shown in Figures 1 and 2, respectively, while the selected bond distances and angles are given in Table 2. Both the complexes contain two crystallographically independent molecules in the unit cell. The stereochemical dispositions of the chelating units around the metal centers depict homochirality, and therefore, the diastereoisomer should be regarded as the *rac* (ΛΛ/ΔΔ) form. The structures of both the complexes consist of two hexa-coordinated metal(II) centers in which the two $\mathrm{M(bpy)_2}$ units are bridged by the imidazolate nitrogens N(9) and N(10) of Imdc(3−) and the carboxylate oxygens O(1) and O(3) complete the octahedron. The coordination environment around each metal center in both

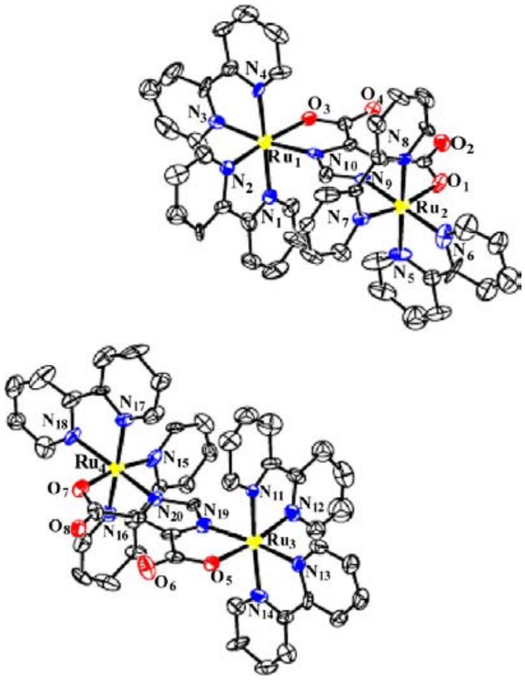

Figure 1. ORTEP representations of the $[(bpy)_2Ru(Imdc)Ru(bpy)_2]^+$ cation in **1** showing 40% probability of thermal ellipsoid. H atoms have been omitted for clarity.

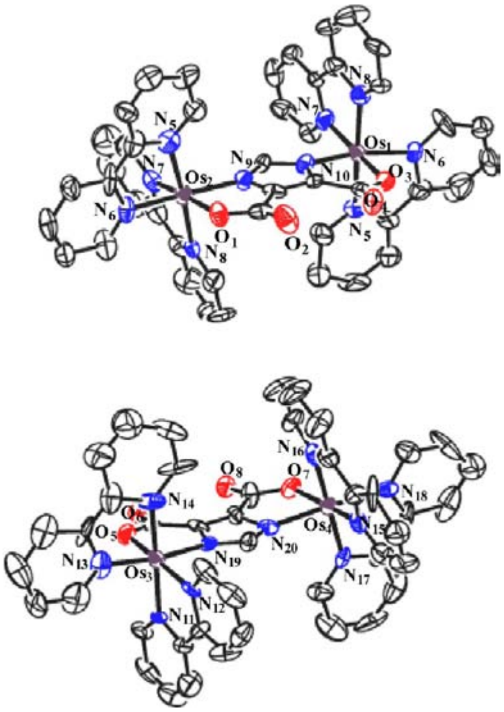

Figure 2. ORTEP representations of the $[(bpy)_2Os(Imdc)Os(bpy)_2]^+$ cation in **2** showing 40% probability of thermal ellipsoid. H atoms have been omitted for clarity.

1 and **2** are distorted octahedrals, and the deviations of the metal centers from idealized octahedral geometry are reflected in their bond angles: the *cis* angles vary from 77.95(3) to 81.61(3)° for **1** and from 77.64(3) to 79.36(3)° for **2**, while the *trans* angles lie between 169.71(3) and 178.02(3)° for **1** and between 168.43(3) and 175.16(3)° for **2**. The average Ru−N(bpy), Ru−N-(imidazolate), and Ru−O(carboxylate) distances in **1** are 2.03(2), 2.04(1), and 2.08(2) Å, respectively. The corresponding distances observed for the diosmium(II) analogue (**2**) are almost the same, viz. 2.03(1), 2.04(1), and 2.07(1) Å. It is also of interest to note that the nonbonded Os−Os separation of 6.261 Å in **2** is slightly longer compared to the Ru−Ru distance of 6.251 Å in **1**, indicating slightly tighter bonding in the ruthenium compound. It may also be noted that the shorter average C−O distance of the free carbonyl moiety of $Imdc^{3-}$ [1.214 Å for **1** and 1.188 Å for **2**] relative to that of the metal-bound C−O [1.320 Å for **1** and 1.278 Å for **2**] is consistent with pronounced double bond character of the former. In both the structures, it is seen that the two >C=O groups adopt a *syn* arrangement, and this pair of externally directed >C=O groups of $Imdc^{3-}$ could be used for the formation of adduct with the incoming cationic guests (Chart 1).

Ground-State Structural and Electronic Properties. Computational studies were carried out on the ground states of the complexes **1**, **2**, [**1·H**], [**2·H**], [**1·Li**], [**1·Li·1**], and [**2·Li·2**]. The optimized geometries for the complexes **1** and **2** computed both in the gas and in solution phases are shown in Figure S3 (Supporting Information [SI]), and the geometrical parameters are summarized in Table S1 (SI). The optimized geometries for [**1·H**] and [**2·H**], computed in the solution phases only, are shown in Figure S4 (SI), while those of [**1·Li·1**] and [**2·Li·2**] are presented in Figure 3. The geometrical parameters for **1**, [**1·H**], [**1·Li**], and [**1·Li·1**] in acetonitrile are summarized in Table 3, while those for [**2·H**] and [**2·Li·2**] are gathered in Table S2 (SI). The numbering systems for the complexes are the same as that used for the crystal structure analysis.

The calculated structures of the complexes **1** and **2** are distorted octahedrals with M−N and M−O bond lengths slightly elongated compared to those of the crystal structures. All the computed distances are within the experimental error (±0.06 Å). This accuracy is the one expected for the method, taking also into account experimental factors (e.g., crystal packing forces and absence of counteranions) that occasionally can be responsible for apparent discrepancies. The adjacent N−M−N bond angles in the gas phase calculation range from 77.63° to 102.43°, and are all within one degree deviation of the corresponding observed bond angles in the crystal structures.

The optimized structures of the pentameric adducts [**1·Li·1**] and [**2·Li·2**] (Figure 3) show that Li^+ ion is tetrahedrally surrounded by four oxygen atoms derived from two parent dimeric species. The calculated M−N and M−O bond distances in the protonated ([**1·H**] and [**2·H**]), lithiated trimetallic adduct [**1·Li**] as well as Li-coordinated pentameric adducts remain almost the same as those of the free bimetallic host complexes **1** and **2**. By contrast, the calculated C−O bond lengths (1.27 Å) in the above-mentioned adducts are slightly elongated compared to those of the free C−O bonds (1.23 Å) of the parent bimetallic host complexes **1** and **2**. This is quite expected as the free oxygen atoms in the hosts are now involved in the bond formation with the cationic guest.

The frontier orbital of the complexes **1** and **2** in both the gaseous as well as solution phases are shown in Figure 4 and Figure S5 (SI), whereas the orbital energies and compositions in terms of atomic contributions are reported in Table S3 (SI). The assignment of the type of each MO was made on the basis of its composition and by visual inspection of its three-dimensional representation.[44−47] In our calculations, it seen that the highest occupied MOs (HOMO, HOMO−1, HOMO−2, and HOMO−3) in both complexes are mainly ruthenium and osmium d-orbital in character but significant contributions (9−45%) come

Table 2. Selected X-ray Crystallographic Bond Distances (Å) and Angles (deg) for 1 and 2

Bond Distances							
1				2			
Ru1−N1	1.984(16)	Ru2−N5	2.035(9)	Os1−N1	2.009(14)	Os2−N5	2.078(15)
Ru1−N2	2.043(17)	Ru2−N6	2.041(11)	Os1−N2	1.993(13)	Os2−N6	2.015(12)
Ru1−N3	2.083(12)	Ru2−N7	2.016(12)	Os1−N3	2.050(13)	Os2−N7	2.043(11)
Ru1−N4	2.070(12)	Ru2−N8	2.022(11)	Os1−N4	2.028(14)	Os2−N8	2.020(12)
Ru1−N10	2.058(10)	Ru2−N9	2.041(9)	Os1−N10	2.036(13)	Os2−N9	2.046(12)
Ru1−O3	2.098(11) Ru2−O1	Ru2−O1	2.071(9)	Os1−O3	2.091(9)	Os2−O1	2.056(9)

Bond Angles							
1				2			
O3−Ru1−N1	94.8(6)	O1−Ru2−N5	90.7(4)	O3−Os1−N1	94.5(4)	O1−Os2−N5	87.4(5)
O3−Ru1−N2	173.1(5)	O1−Ru2−N6	95.3(4)	O3−Os1−N2	170.7(5)	O1−Os2−N6	94.5(4)
O3−Ru1−N3	94.0(4)	O1−Ru2−N7	169.7(4)	O3−Os1−N3	91.5(4)	O1−Os2−N7	171.2(6)
O3−Ru1−N4	90.7(5)	O1−Ru2−N8	90.6(4)	O3−Os1−N4	90.2(5)	O1−Os2−N8	92.8(5)
O3−Ru1−N10	77.9(4)	O1−Ru2−N9	79.1(4)	O3−Os1−N10	78.7(4)	O1−Os2−N9	77.7(4)
N2−Ru1−N1	78.3(7)	N6−Ru2−N5	79.5(4)	N2−Os1−N1	78.2(5)	N6−Os2−N5	77.7(7)
N2−Ru1−N3	87.2(5)	N6−Ru2−N7	92.7(4)	N2−Os1−N3	95.2(4)	N6−Os2−N7	90.5(4)
N2−Ru1−N4	96.2(6)	N6−Ru2−N8	99.0(4)	N2−Os1−N4	97.4(5)	N6−Os2−N8	97.5(6)
N2−Ru1−N10	101.5(5)	N6−Ru2−N9	170.4(4)	N2−Os1−N10	95.2(4)	N6−Os2−N9	172.0(4)
N3−Ru1−N1	101.0(5)	N7−Ru2−N5	97.2(4)	N3−Os1−N1	97.3(6)	N7−Os2−N5	100.8(5)
N3−Ru1−N4	78.8(5)	N7−Ru2−N8	81.6(4)	N3−Os1−N4	78.3(5)	N7−Os2−N8	79.4(5)
N3−Ru1−N10	170.2(5)	N7−Ru2−N9	93.9(4)	N3−Os1−N10	168.4(5)	N7−Os2−N9	97.5(4)
N10−Ru1−N1	85.4(5)	N9−Ru2−N5	92.7(4)	N10−Os1−N1	89.7(5)	N9−Os2−N5	99.7(6)
N10−Ru1−N4	95.5(4)	N9−Ru2−N8	88.9(4)	N10−Os1−N4	95.4(5)	N9−Os2−N8	85.0(5)
N1−Ru1−N4	174.5(6)	N8−Ru2−N5	178.1(4)	N1−Os1−N4	173.7(5)	N8−Os2−N5	175.2(6)

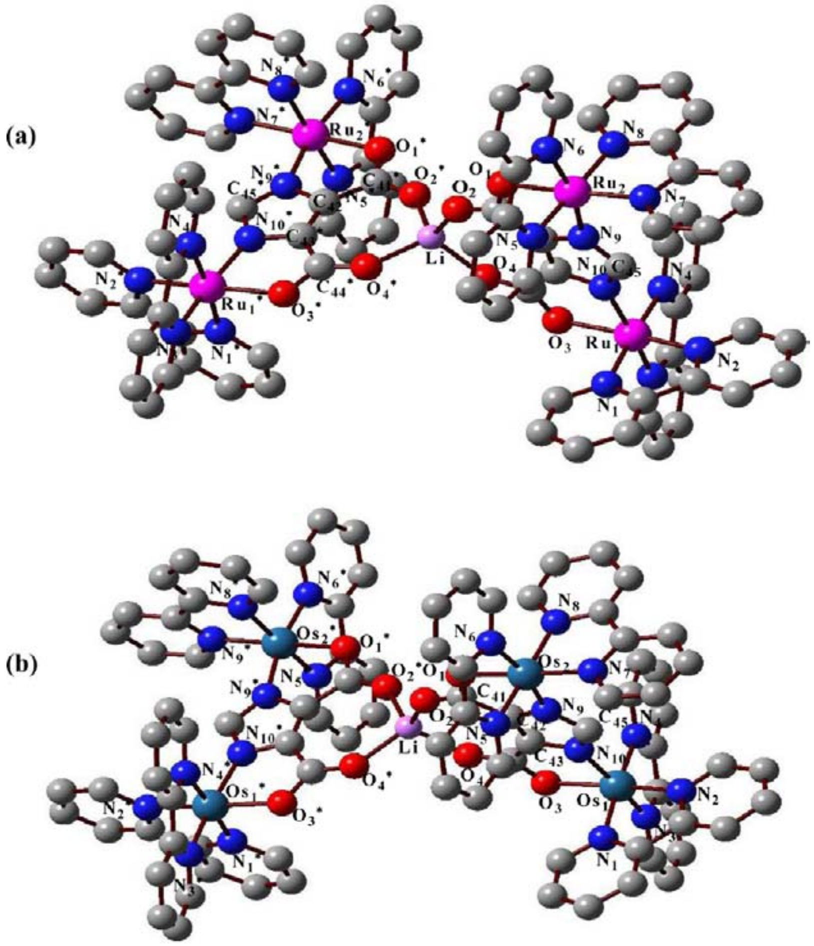

Figure 3. Optimized geometries and labeling schemes of [**1·Li·1**] (a) and [**2·Li·2**] (b) in solution phase.

Table 3. Selected Calculated Bond Distances (Å) and Angles (deg) for 1, [1·H], [1·Li], and [1·Li·1] in Acetonitrile in Singlet and Triplet States

	1			**[1·H]**			**[1·Li]**			**[1·Li·1]**		
	^{1}A	^{3}A		^{1}A	^{3}A		^{1}A	^{3}A		^{1}A	^{3}A	
		UKS	TD-DFT		UKS	TD-DFT		UKS	TD-DFT		UKS	TD-DFT
Ru1–N1	2.074	2.077	2.077	2.079	2.070	2.091	2.072	2.067	2.085	2.073	2.071	2.077
Ru1–N2	2.074	2.074	2.074	2.063	2.069	2.013	2.059	2.046	2.014	2.059	2.074	2.068
Ru1–N3	2.087	2.085	2.085	2.081	2.100	2.083	2.082	2.092	2.086	2.080	2.106	2.087
Ru–N4	2.087	2.088	2.089	2.094	2.113	2.107	2.088	2.11	2.103	2.086	2.109	2.091
Ru1–N10	2.084	2.088	2.088	2.110	2.057	2.106	2.087	2.071	2.084	2.089	2.034	2.088
Ru1–O3	2.112	2.116	2.116	2.165	2.149	2.122	2.152	2.119	2.116	2.148	2.127	2.126
Ru2–N5	2.087	2.108	2.102	2.098	2.114	2.098	2.088	2.091	2.089	2.086	2.110	2.090
Ru2–N6	2.08	2.099	2.098	2.084	2.095	2.083	2.082	2.081	2.08	2.080	2.106	2.087
Ru2–N7	2.074	2.074	2.044	2.055	2.055	2.054	2.059	2.059	2.059	2.059	2.075	2.068
Ru2–N8	2.074	2.083	2.098	2.081	2.070	2.082	2.072	2.074	2.073	2.073	2.071	2.077
Ru2–N9	2.084	2.074	2.081	2.111	2.065	2.113	2.087	2.088	2.09	2.089	2.033	2.090
Ru2–O1	2.112	2.048	2.047	2.192	2.206	2.196	2.152	2.156	2.156	2.148	2.124	2.126
Li–O2	–	–	–	–	–	–	1.865	1.873	1.870	1.921	1.921	1.921
Li–O4	–	–	–	–	–	–	1.865	1.886	1.888	1.920	1.928	1.920
	1			**[1·H]**			**[1·Li]**			**[1·Li·1]**		
	^{1}A	^{3}A		^{1}A	^{3}A		^{1}A	^{3}A		^{1}A	^{3}A	
		UKS	TD-DFT		UKS	TD-DFT		UKS	TD-DFT		UKS	TD-DFT
O3–Ru1–N1	94.3	94.2	94.2	95.0	96.4	96.4	94.6	96.5	96.3	94.7	96.1	94.8
O3–Ru1–N2	171.4	171.5	171.4	172.3	173.9	174.1	171.9	174.1	173.3	172.0	173.2	174.3
O3–Ru1–N3	92.7	92.4	92.3	92.0	93.1	92.4	93.4	95.7	93.7	93.0	94.2	93.2
O3–Ru1–N4	88.4	88.6	88.8	87.7	85.3	85.4	88.1	84.6	85.3	87.7	86.5	88.0
O3–Ru1–N10	77.7	77.8	77.8	78.5	79.8	78.6	77.5	77.8	77.3	77.6	78.7	77.5
N2–Ru1–N1	78.4	78.4	78.4	78.6	78.9	80.1	79.1	80.2	80.6	79.0	79.0	78.6
N2–Ru1–N3	92.8	92.8	92.9	93.1	91.3	92.8	92.3	89.7	92.6	92.7	91.0	92.6
N2–Ru1–N4	99.1	98.9	98.9	98.9	99.7	98.4	98.6	99.1	98.2	98.8	98.9	99.1
N2–Ru1–N10	97.5	97.7	97.6	96.9	96.2	96.3	97.4	97.1	96.5	97.2	96.5	97.4
N3–Ru1–N1	98.1	98.1	98.1	97.7	96.4	98.5	97.4	97.3	97.7	97.3	96.4	98.0
N3–Ru1–N4	78.2	78.2	78.2	78.3	77.7	78.3	78.7	78.3	78.8	78.7	77.6	78.2
N3–Ru1–N10	168.5	168.1	168.1	169.0	171.3	170.7	169.2	172.6	170.6	169.0	171.2	168.9
N10–Ru1–N1	89.0	89.4	89.4	88.9	89.4	85.1	89.2	86.8	86.1	89.1	89.6	88.9
N10–Ru1–N4	95.1	94.7	94.7	95.5	96.6	98.3	95.1	97.7	97.5	95.1	96.6	95.3
O1–Ru2–N5	88.4	85.8	86	87.4	86.1	87.4	88.1	87.7	87.9	87.7	86.4	88.0
O1–Ru2–N6	92.7	94.2	93.1	92.9	94.5	92.7	93.4	93.4	93.2	93.0	93.9	93.0
O1–Ru2–N7	171.4	174.7	173.8	172.5	173.2	172.5	171.9	172.3	172.1	172.0	173.2	171.8
O1–Ru2–N8	94.3	96.8	97	95.6	96.5	95.6	94.6	94.9	94.8	94.7	96.1	94.9
O1–Ru2–N9	77.7	78.4	78	78.0	78.6	77.9	77.5	77.5	77.5	77.6	78.7	77.4
N6–Ru2–N5	78.2	77.8	78	78.2	77.7	78.3	78.7	78.7	78.7	78.7	77.6	78.2
N6–Ru2–N7	92.8	89.9	92.5	92.8	91.4	92.9	92.3	92.2	92.3	92.7	91.3	92.7
N6–Ru2–N8	98.1	98.8	99.3	97.6	95.9	97.5	97.4	97.3	97.3	97.4	96.4	98.1
N6–Ru2–N9	168.5	171.9	170.7	169.4	171.6	169.0	169.2	169.4	169.2	169.0	170.9	168.7
N7–Ru2–N5	99.1	98.4	97.9	98.7	98.6	98.6	98.5	98.6	98.6	98.8	99.0	99.0
N7–Ru2–N8	78.4	79.1	79.4	78.7	79.4	78.8	79.1	79	79.1	79.0	79.0	78.5
N7–Ru2–N9	97.5	97.7	96.5	96.8	95.8	97.0	97.4	97.4	97.4	97.2	96.5	97.4
N9–Ru2–N5	95.1	98.4	98.7	95.8	97.0	95.4	95.1	95.3	95.24	95.1	96.5	95.3
N9–Ru2–N8	89.0	85.3	84.4	88.7	89.6	89.2	89.2	89	89.2	89.1	89.8	88.8
O2–Li–O4	–	–	–	–	–	–	109.6	108.9	109.1	105.8	105.4	106.2

from the p orbitals of the imidazole-dicarboxylate (Imdc^{3-}) moiety. The contributions of the bpy in the HOMOs are much less, as expected. On the other hand, all the lowest unoccupied molecular orbitals (LUMO, LUMO+1, LUMO+2, and LUMO+3) are mainly (86.8–93.7%) composed of bpy in both complexes. Our results are also in agreement with the DFT study[44–56] of homo- and heteroleptic polypyridyl complexes of Ru(II) and Os(II), wherein the highest occupied MOs were mainly of metal d-orbital origin and were π antibonding, yet had significant density on the coligands. On the other hand, the LUMO and subsequent virtual (unoccupied) orbitals are essentially π^* orbitals of the polypyridyl moieties. It is of interest to note that on going from the gaseous to the solution phase, contributions of the metals (ruthenium and osmium) in the HOMOs increase, while the contribution of Imdc^{3-} decreases slightly [Figure 4, Figure S5 and Table S3 (SI)]. The bpy contributions in the LUMOs on the other hand remain almost unaltered on going from gas to solution.

The frontier orbitals of [**1**·Li·**1**] and [**2**·Li·**2**] in solution phase are shown in Figure 5, while those of [**1**·H], [**2**·H], and [**1**·Li] are

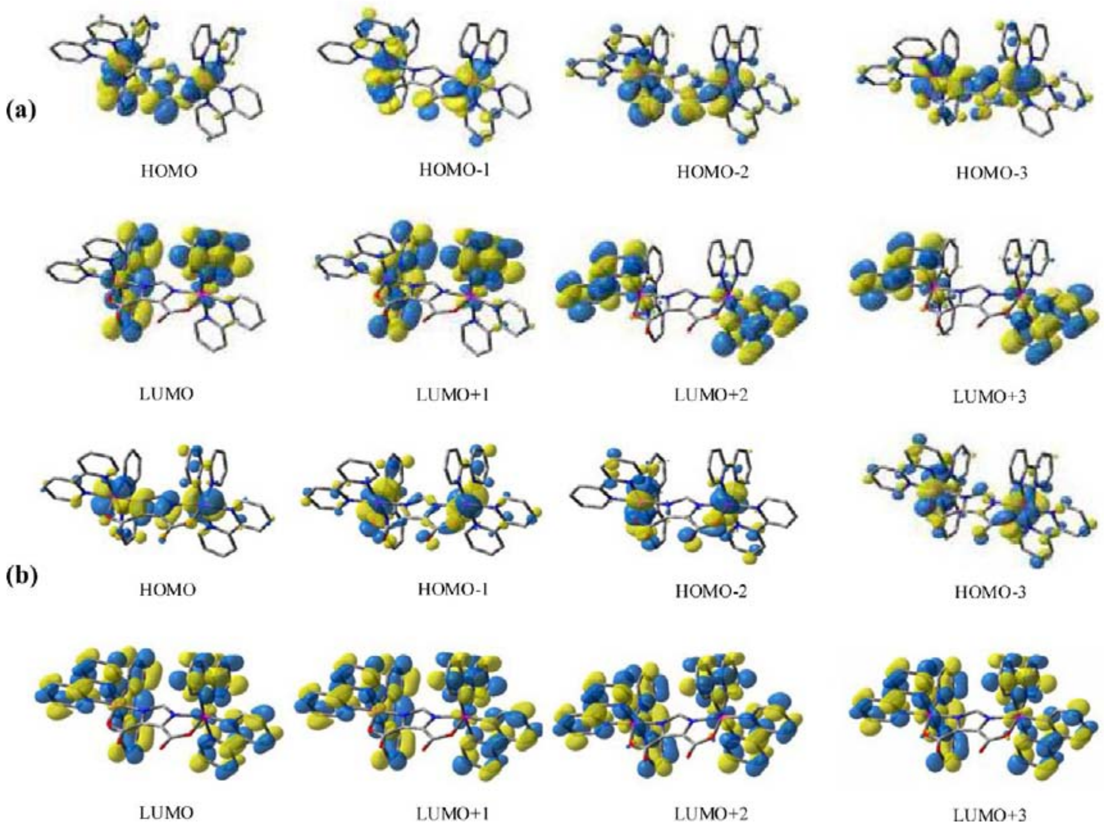

Figure 4. Schematic drawings of the selective frontier molecular orbitals for **1** in gas (a) and solution phase (b).

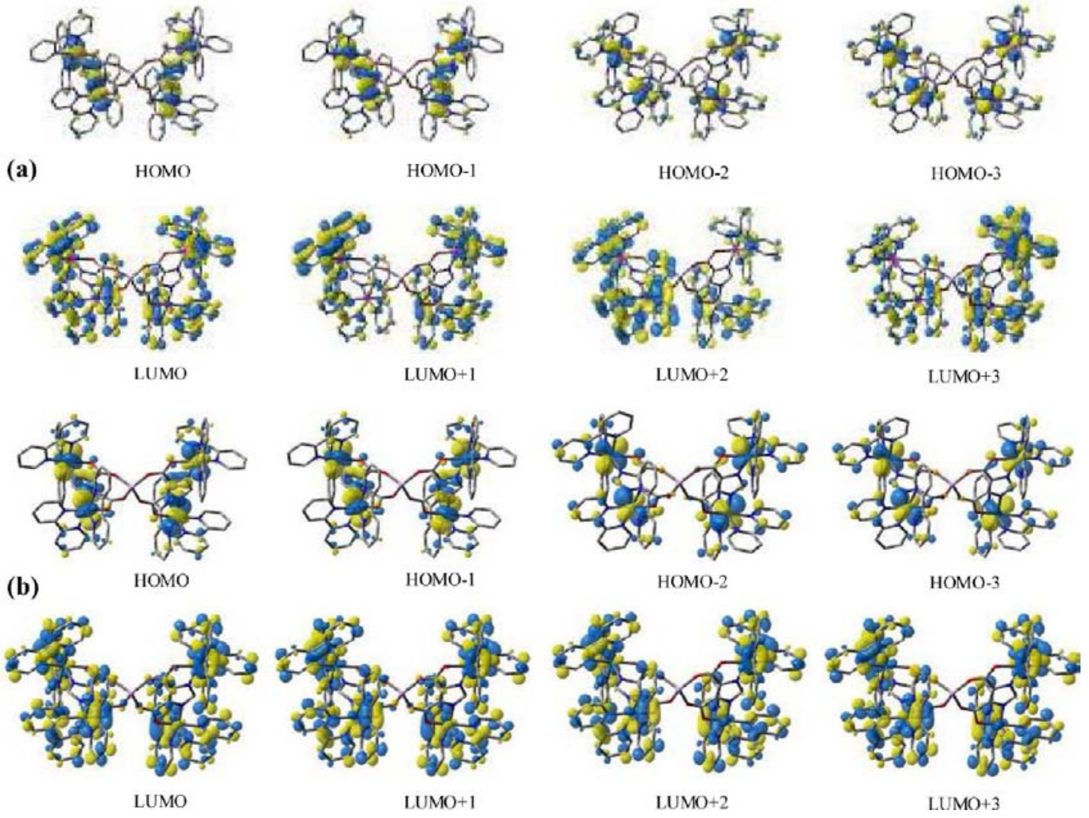

Figure 5. Schematic drawings of the selective frontier molecular orbitals for [**1**·**Li**·**1**] (a) and [**2**·**Li**·**2**] (b) in solution phase.

presented in Figures S6–S7 (SI). The orbital energies and compositions for **1**, [**1**·**H**], [**1**·**Li**], and [**1**·**Li**·**1**] in terms of atomic contributions are reported in Table 4, while those for [**2**·**H**] and [**2**·**Li**·**2**] are gathered in Table S4 (SI). From Table 4,

Table 4. Selected MOs along with their Energies and Compositions for **1**, [**1**·**H**], [**1**·**Li**], and [**1**·**Li**·**1**] in Acetonitrile

		(%) composition			
MO	energy/eV	Ru^{II}	Li^{I}[a]	Imdc^{3-}	bpy
1					
HOMO−3	−5.352	72.1	–	12.6	15.3
HOMO−2	−5.311	75.6	–	12.3	12.1
HOMO−1	−5.263	78.3	–	9.2	12.6
HOMO	−5.225	76.4	–	12.7	10.9
LUMO	−2.243	5.4	–	0.9	93.7
LUMO+1	−2.241	6.6	–	0.6	92.8
LUMO+2	−2.154	9.4	–	1.1	89.5
LUMO+3	−2.142	9.4	–	1.1	89.6
[**1**·**H**]					
HOMO−3	−5.859	79.5	–	4.8	15.6
HOMO−2	−5.775	78.4	–	7.2	14.4
HOMO−1	−5.693	79.0	–	7.7	13.4
HOMO	−5.615	80.2	–	8.2	11.6
LUMO	−2.454	5.0	–	1.7	93.2
LUMO+1	−2.395	5.6	–	1.4	93.0
LUMO+2	−2.375	8.4	–	1.0	90.5
LUMO+3	−2.314	8.6	–	1.0	90.4
[**1**·**Li**]					
HOMO−3	−5.829	70.7	0.00	10.1	19.1
HOMO−2	−5.799	72.5	0.01	9.4	18.5
HOMO−1	−5.692	76.0	0.01	6.7	17.0
HOMO	−5.628	71.7	0.00	12.3	16.0
LUMO	−2.602	3.0	0.00	1.9	95.3
LUMO+1	−2.599	3.4	0.02	0.8	92.2
LUMO+2	−2.509	7.2	0.11	0.9	91.8
LUMO+3	−2.494	7.5	0.00	1.0	91.6
[**1**·**Li**·**1**]					
HOMO−3	−5.642	75.3	0.02	7.0	17.7
HOMO−2	−5.64	75.1	0.02	7.2	17.7
HOMO−1	−5.583	71.7	0.00	12.4	15.9
HOMO	−5.582	71.5	0.01	12.6	15.9
LUMO	−2.579	3.3	0.01	1.6	95.1
LUMO+1	−2.578	3.4	0.00	1.4	95.2
LUMO+2	−2.578	3.7	0.01	0.8	95.5
LUMO+3	−2.578	3.6	0.03	1.0	95.4

[a] As the contribution of Li$^+$ ion is very small, 2 decimal digits were given.

Tables S3−S4 (SI), Figures 4 and 5 and Figure S5 (SI), it can be seen that there are obvious differences in the compositions and shapes of the different frontier orbitals between the free bimetallic host (**1** and **2**) and the pentametallic adducts [**1**·**Li**·**1**] and [**2**·**Li**·**2**]. It is of interest to note that on going from the free to the corresponding pentametallic adducts, metal (ruthenium and osmium) contribution in HOMO, HOMO−1, and HOMO−2 decreases, while in HOMO−3, it increases slightly in both cases. On the other hand, bpy contribution increases in all four HOMOs in both [**1**·**Li**·**1**] and [**2**·**Li**·**2**]. For HOMO−1, the contribution of bpy and Imdc^{3-} increases remarkably from 16.6 to 43.9 and from 8.7 to 24.0, respectively, on passing from **2** to [**2**·**Li**·**2**], while the contribution of Imdc^{3-} decreases substantially in HOMO−2 and HOMO−3 on going from both **1** to [**1**·**Li**·**1**] and **2** to [**2**·**Li**·**2**]. It is worth noting that there is very small but finite contribution of Li$^+$ ion in all the HOMOs and LUMOs in both [**1**·**Li**·**1**] and [**2**·**Li**·**2**]. On going from **1** to [**1**·**Li**·**1**], the bpy contribution in the LUMOs increases, while contribution of Ru^{II} decreases; Imdc^{3-} contribution, on the other hand, increases in LUMO and LUMO+1, while it decreases slightly in LUMO+2 and LUMO+3. However, on going from **2** to [**2**·**Li**·**2**], the bpy contribution decreases slightly in LUMO and LUMO+1, while it increases slightly in LUMO+2 and LUMO+3. The contribution of Os^{II} decreases in the LUMOs on going from **2** to [**2**·**Li**·**2**] similar to the case of **1**. It may be mentioned that in contrast to both [**1**·**Li**·**1**] and [**2**·**Li**·**2**], there is an increase in the contribution of the metal in the HOMOs on going from **1** to [**1**·**H**] or **2** to [**2**·**H**], while the bpy contribution in the HOMOs as well as LUMOs remains almost the same. From Table 4, Figure 5, and Figure S7 (SI), it can be seen that there are small but finite differences in the compositions and shapes of the different frontier orbitals between [**1**·**Li**] and [**1**·**Li**·**1**]. It is also of interest to note that the contributions of Li$^+$ ion in all the HOMOs are relatively smaller in [**1**·**Li**] than in [**1**·**Li**·**1**].

In order to check the probable formation of either [**1**·**Li**] or [**1**·**Li**·**1**] on interaction of **1** with the Li$^+$ ion, we have calculated the formation energies of **1**, [**1**·**Li**], and [**1**·**Li**·**1**] by performing thermochemical analysis on the optimized geometries of the respective species. Now, by comparing the sum of electronic and thermal free energy of **1** (−2772.5 hartree), [**1**·**Li**] (−2777.6 hartree), and [**1**·**Li**·**1**] (−5547.7 hartree), it can be concluded that the formation of the pentameric species ([**1**·**Li**·**1**]) is more probable than the trimetallic adduct ([**1**·**Li**]). As will be seen later, the experimental evidence (^{1}H NMR, absorption, and emission titration experiments) also suggests the formation of the pentametallic species over the trimetallic one.

Proton NMR Spectra. ^{1}H NMR spectroscopy has been useful to ascertain diastereoisomeric purity of the dinuclear complexes isolated. Since the chemical shift of the imidazolate CH proton of the bridging (Imdc^{3-}) ligand should show small

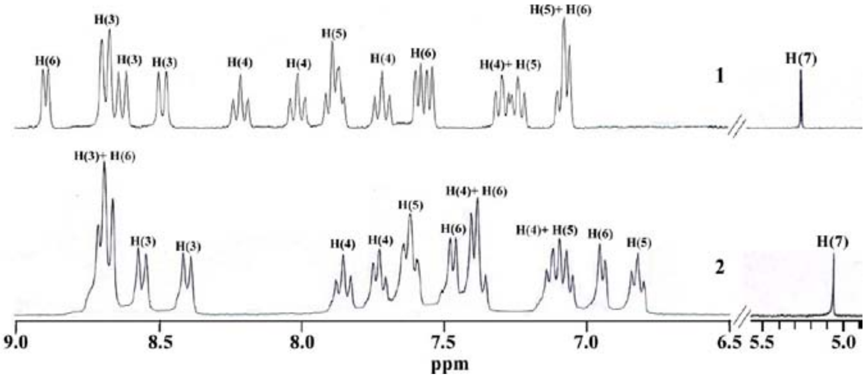

Figure 6. ^{1}H NMR (300 MHz) spectra of **1** and **2** in DMSO-d_6. Atoms numbering for the complexes are shown in Chart 1.

but definite differences for the diastereoisomers, the occurrence of a lone singlet due to Imz-CH will characterize the species as a single diastereoisomer. The ^{1}H NMR spectra of **1** and **2** are shown in Figure 6. It may be noted that only one singlet is observed at 5.26 ppm for **1** and at 5.06 ppm for **2**, thus clearly establishing the diastereomeric purity of the compounds. The assignments of the resonances due to the bipyridines in the complexes have been aided by their $\{^1H-^1H\}$ COSY spectra (Figures S8 and S9, SI). The assignments made in this way for both compounds are already given in the Experimental Section.

Electronic Absorption Spectroscopic Studies. The UV–vis spectra of the complexes are shown in Figure 7, and their absorption maxima and molar extinction coefficients (ε) in acetonitrile are given in the Experimental Section. The absorption spectra of the complexes are of similar type showing a number of bands in the UV–vis region. On the basis of the extensive investigations performed on $[M(bpy)_3]^{2+}$ ($M = Ru^{II}$ and Os^{II}) and related tris-bidentate Ru(II) and Os(II) complexes[1,10,14] it can be surmised that the high-intensity absorption bands in the 200–400 nm (ε = 16740–82380 M^{-1} cm^{-1}) spectral region are due to $\pi-\pi^*$ transition of bipyridine and spin-allowed ligand-centered (LC) transitions of the bridging Imdc^{3-} ligand. The absorption band and shoulder in the 400–600 nm (ε = 9380–15600 M^{-1} cm^{-1}) region are due to spin-allowed metal-to-ligand $^1[M^{II}(d\pi)^6] \rightarrow {}^1[M^{II}(d\pi)^5bpy(\pi^*)^1]$ charge–transfer (MLCT) transitions. The Os(II) compound **2**, additionally shows moderately intense broad bands around 805 (ε = 3800 M^{-1} cm^{-1}) and 710 (ε = 4700 M^{-1} cm^{-1}) which seems to be due to spin forbidden MLCT transition $^1[Os^{II}(d\pi)^6] \rightarrow {}^3[Os^{II}(d\pi)^5bpy(\pi^*)^1]$ that directly populates the triplet MLCT state.[1] It is of interest to note that the lowest energy ^{1}MLCT absorption band for the complexes is shifted to longer wavelength compared to the parent $[Ru(bpy)_3]^{2+}$ (451 nm) and $[Os(bpy)_3]^{2+}$ (477 nm) complexes indicating better σ-/π-donor ability of the bridging 4,5-imidazole-dicarboxylate ligand compared to bipyridine. The Os(II) system in the present study is of particular interest because its absorption spectrum covers almost the entire visible range of the electromagnetic spectrum. Such a black absorber may be a promising candidate to replace conventional Ru(II)-bipyridine dyes which present a typical absorption maximum centered below 550 nm.[2−4]

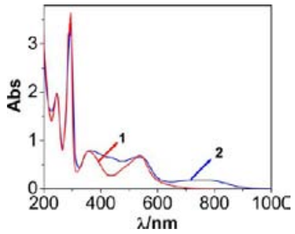

Figure 7. Absorption spectra of **1** (red) and **2** (blue) in acetonitrile at room temperature.

Emission Spectroscopic Studies. The luminescence spectra of the complexes in acetonitrile at room temperature and in EtOH–MeOH (4:1 v/v) glass at 77 K are presented in Figure 8. At room temperature, complex **1** in acetonitrile on excitation at 480 and 538 nm, where the two MLCT absorption maxima are observed, exhibits one broad luminescent band with the peak at 770 nm. This band position remains unchanged when λ_{ex} is varied between 480 and 538 nm. Again, on the basis of extensive investigations performed on $[M(bpy)_3]^{2+}$ and related complexes, it can be concluded that these bands have the characteristics of emission from the ^{3}MLCT excited state, which corresponds to a spin-forbidden $M^{II}(d\pi) \rightarrow bpy(\pi^*)$ transition.[1,10,14] The analogous Os(II) complex **2**, however does not exhibit luminescence at room temperature. When the measurements are carried out at 77 K, complex **2** shows some luminescence with its peak at 715 nm. In the case of **1**, on going from fluid solution to frozen glass, the emission maximum gets blue-shifted with a significant increase of emission intensity and quantum yield, typical of the ^{3}MLCT emitters.[1,10] The zero–zero excitation energy (E_{00}) values of the ^{3}MLCT excited state of the complexes are 1.79 eV for **1** and 1.74 eV for **2**, estimated from the emission maximum at 77 K. At 77 K, the emission spectrum displays a well-defined vibronic progression in the lower-energy region with spacing of ~1310 cm^{-1} for **1** and ~916 cm^{-1} for **2** which are similar to those reported for $[M(bpy)_3]^{2+}$ and related compounds and can be attributed to aromatic stretching vibrations of the ligands.[1,10,57]

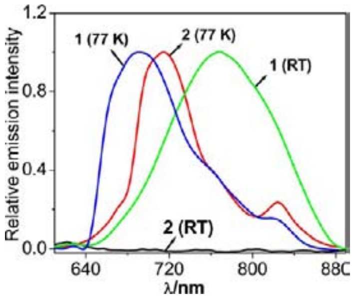

Figure 8. Normalized photoluminescence spectra of **1** and **2** at room temperature in acetonitrile and at 77 K in ethanol–methanol (4:1 v/v) glass.

Electrochemical Properties. The electrochemical characteristics of the complexes have been examined by cyclic voltammetry (CV) and square wave voltammetry (SWV) in CH_3CN solutions, and the cyclic voltammograms of both the complexes are shown in Figure 9. Both the complexes are found to undergo two successive one-electron reversible oxidations in the positive potential window (0 to +1.2 V) and two successive quasi-reversible reductions in the negative potential window (0 to −2.2 V) (Figure S10, SI). In polypyridyl complexes of ruthenium(II) and osmium(II) the highest occupied molecular orbitals (HOMO) are normally localized on the metal center, and oxidative processes are therefore metal based, whereas the lowest unoccupied molecular orbitals (LUMO) are usually ligand based, and the reduction processes are therefore ligand

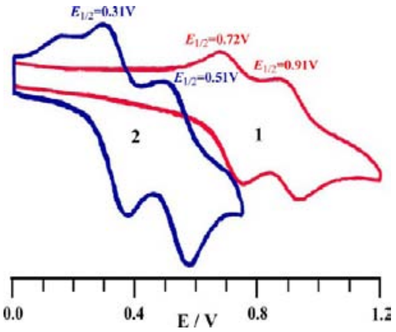

Figure 9. Cyclic voltammograms of **1** and **2** recorded at a scan rate of 100 mV s^{-1} in acetonitrile at room temperature using Ag/AgCl as the reference and platinum as the working electrode.

centered, in agreement with literature data and the reversibility of most of the processes.[1,10,58] Thus, the reversible oxidations at 0.72 and 0.91 V for **1** have been assigned as $\mathrm{Ru^{II}Ru^{II}/Ru^{II}Ru^{III}}$ and $\mathrm{Ru^{II}Ru^{III}/Ru^{III}Ru^{III}}$ processes, while the oxidations at 0.31 and 0.51 V for **2** can been assigned as $\mathrm{Os^{II}Os^{II}/Os^{II}Os^{III}}$ and $\mathrm{Os^{II}Os^{III}/Os^{III}Os^{III}}$ processes. It may be noted that the oxidation potential of the $\mathrm{Os^{II}/Os^{III}}$ couple in **2** is less positive compared to the $\mathrm{Ru^{II}/Ru^{III}}$ couple in **1**, consistent with the greater stability of a third-row transition metal ion vis-à-vis a second-row metal ion in higher oxidation states. It is interesting to note that the separation between $E_{1/2}(2)$ and $E_{1/2}(1)$, $\Delta E_{1/2}$, is almost identical for **1** (0.19 V) and **2** (0.20 V). Accordingly, the equilibrium constant K_c for the comproportionation reaction, $\mathrm{M^{II}M^{II} + M^{III}M^{III} \rightleftharpoons 2M^{II}M^{III}}$ ($K_c = \exp[nF\Delta E_{1/2}/RT]$), is almost identical for the two systems [1.6×10^3 for **1** and 2.3×10^3 for **2**]. The magnitude of K_c indicates that the mixed-valence $\mathrm{M^{II}M^{III}}$ species belong to class II system of the Robin–Day classification[59] for which K_c typically lies in the range 10^2–10^6.[60] The reduction processes of the complexes were observed at −1.36 and −1.68 V for **1** and −1.49 and −1.77 V for **2**, being assigned as bpy-centered processes by comparing the reduction potential of $[\mathrm{M(bpy)_3}]^{2+}$ and related diruthenium(II) and diosmium(II) complexes of other electron-rich imidazole-containing bridging ligands.[10,14] The current heights of these two waves indicate that they correspond to simultaneous two-electron transfer processes.

Cation Binding Properties of the Complexes. As already mentioned in the Introduction, two free >C═O groups in the metal complexes adopt a *syn* arrangement, and this pair of externally directed O atoms of the coordinated imidazole-4,5-dicarboxylate moiety ($\mathrm{Imdc^{3-}}$) could be used as the trap for the cationic guests. The binding of the cationic guests with the host bimetallic Ru(II) and Os(II) complexes have been followed spectrophotometrically by observing the spectral changes that occur on the incremental addition of the metal ion to the solutions of the host complexes until no further change is noted. Parts a–c of Figure 10 show the spectral changes that take place upon the addition of increased amounts of $\mathrm{LiClO_4}$, $\mathrm{NaClO_4}$, and $\mathrm{KClO_4}$ to the acetonitrile solution of **1**, respectively. As shown in Figure 10, the absorption peak of **1** at 538 nm becomes blue-shifted with diminution of intensity on the addition of the alkali metal ($\mathrm{Li^+}$ or $\mathrm{Na^+}$) salt. With both $\mathrm{Li^+}$ and $\mathrm{Na^+}$, the successive absorption curves pass through well-defined isosbestic points at 530 and 370 nm for $\mathrm{Li^+}$ and 535 and 372 nm for $\mathrm{Na^+}$ with the development of a new band at 520 and 528 nm, respectively. The insets of a and b of Figure 10 show that the intensity of the new band increases linearly with the incremental addition of both $\mathrm{Li^+}$ and $\mathrm{Na^+}$ ions and becomes maximized when the host-to-cation guest ratio reaches 1:0.6. An even higher amount of the metal ions does not lead to any further change. The extent of change with $\mathrm{K^+}$ is much less compared with the changes with $\mathrm{Li^+}$ and $\mathrm{Na^+}$.

Parts a–c of Figure 11 show the absorption spectral changes upon incremental addition of $\mathrm{Be(ClO_4)_2}$, $\mathrm{Mg(ClO_4)_2}$, and $\mathrm{Ca(ClO_4)_2}$ to the acetonitrile solution of **1**, respectively. As may be noted, augmentation of the intensity of the peak in the range of 500–520 nm at the expense of the diminution of intensities of the lowest energy MLCT peak at 538 nm occurs with the incremental addition of alkaline earth metal. For all three metal ions, successive absorption curves pass through several well-defined isosbestic points (507, 415, and 349 nm for $\mathrm{Be^{2+}}$; 523 and 372 nm for $\mathrm{Mg^{2+}}$; and 525 and 372 nm for $\mathrm{Ca^{2+}}$). The absorption titration profiles of the receptor **1** with the alkaline earth metal ions again show a linear increase of the intensity of new band and thereafter a reasonably sharp end point at a metal/receptor ratio of 0.5:1, indicating the formation of [**1**·$\mathbf{M_1}$·**1**] adduct (Charts 2 and 3).

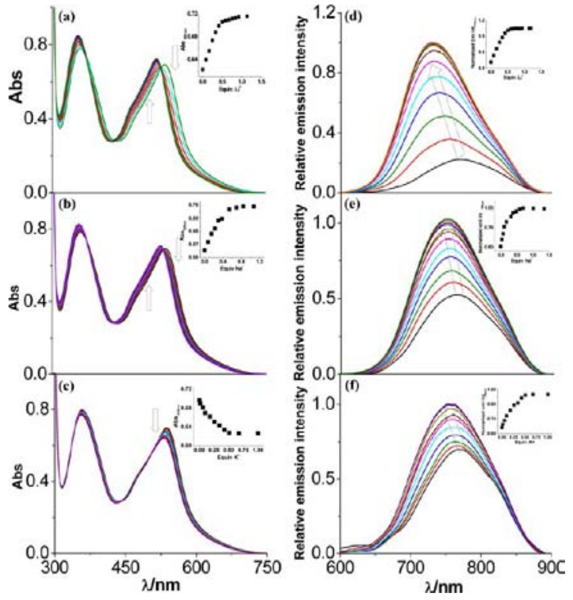

Figure 10. Changes in absorption (a–c) and photoluminescence (d–f) spectra of **1** in acetonitrile solution upon the addition of $\mathrm{Li^+}$, $\mathrm{Na^+}$, and $\mathrm{K^+}$ ion, respectively. Each inset shows the change of absorbance and luminescence intensities as a function of an equivalent of alkali metal cation. The excitation wavelengths are 528, 533, and 505 nm for $\mathrm{Li^+}$, $\mathrm{Na^+}$, and $\mathrm{K^+}$ ion, respectively.

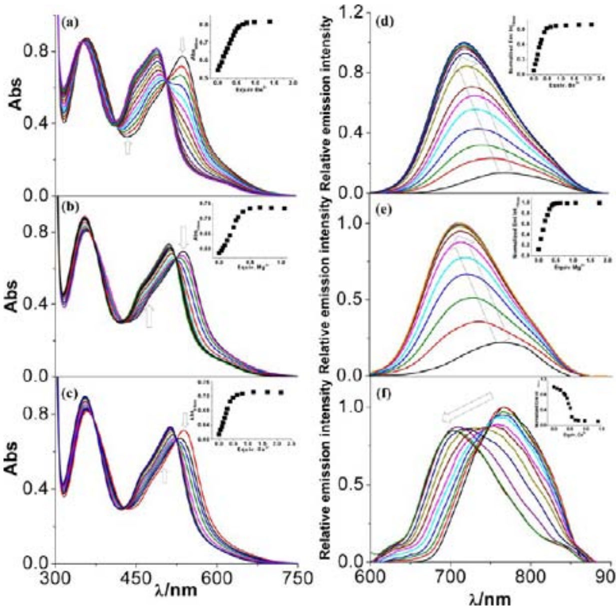

Figure 11. Changes in absorption (a–c) and photoluminescence (d–f) spectra of **1** in acetonitrile solution upon the addition of $\mathrm{Be^{2+}}$, $\mathrm{Mg^{2+}}$, and $\mathrm{Ca^{2+}}$ ion, respectively. Each inset shows the change of absorbance and luminescence intensities as a function of an equivalent of metal ion added. The excitation wavelengths are 508, 523, and 525 nm for $\mathrm{Be^{2+}}$, $\mathrm{Mg^{2+}}$, and $\mathrm{Ca^{2+}}$ ion, respectively.

We will also be interested to see the coordination behavior of the metal ions having a completely filled d orbital (such as $\mathrm{Zn^{2+}}$, $\mathrm{Cd^{2+}}$, or $\mathrm{Hg^{2+}}$). Parts a–c of Figure S11 in the SI show the spectral changes that take place upon the addition of increased

Chart 3

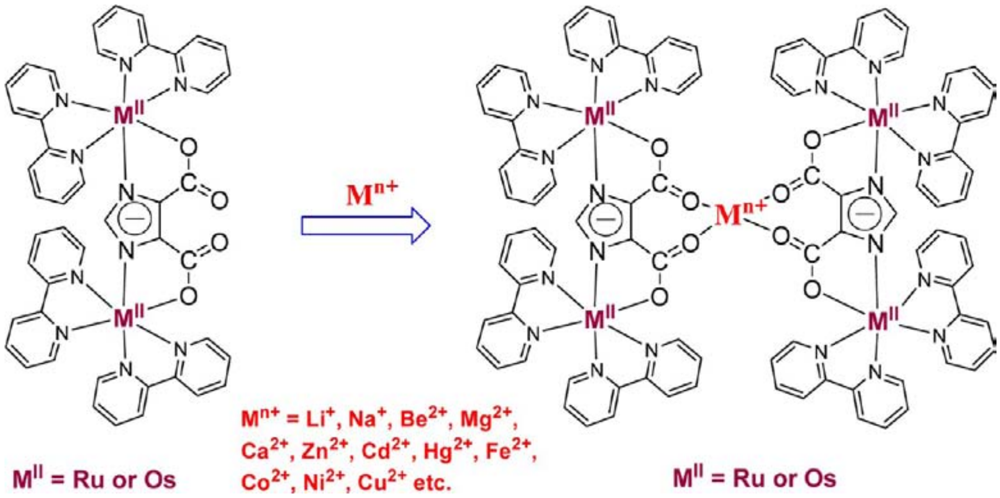

amounts of $Zn(ClO_4)_2$, $Cd(ClO_4)_2$, and $Hg(ClO_4)_2$ to the acetonitrile solution of **1**, respectively. Similar to the case of alkaline earth metals, here also the increase of absorbance around the 500–528 nm region occurs with simultaneous diminution of the intensity of the lowest-energy MLCT peak at 538 nm with the progressive addition of the ions. As in the previous case, the successive absorption curves pass through well-defined isosbestic points (510 and 415 nm for Zn^{2+}; 515, 418, and 362 nm for Cd^{2+}; and 505, 416, and 344 nm for Hg^{2+}). As may be noted in the insets of a–c of Figure S11 (SI), the intensity of the new band increases linearly with the incremental addition of Zn^{2+}, Cd^{2+}, or Hg^{2+} ions until the $[M^{2+}]/[\text{receptor}]$ reaches 0.5.

Figures S12 and S13 (SI) show the spectral changes that take place upon the addition of increased amounts of paramagnetic 3d bivalent metal ions (Mn^{2+}, Fe^{2+}, Co^{2+}, Ni^{2+}, and Cu^{2+}) to the acetonitrile solution of **1**. As may be noted, the new band centered around 486–502 nm increases linearly with the incremental addition of each of the metal ions until the $[M^{2+}]/[\mathbf{1}]$ (M = Mn^{2+}, Fe^{2+}, Co^{2+}, Ni^{2+}, or Cu^{2+}) reaches 0.5. The titration profile and the clear isosbestic points in each case imply the single conversion of **1** to M^{2+} complex of 2:1 stoichiometry. The metal ion binding is also associated with a change of the original color of the free Ru(II) complex (**1**) observable with the naked eye.

The spectral changes that occur for **2** as a function of Zn^{2+}, Cd^{2+}, or Hg^{2+} ions are shown in Figure 12, while those with various alkali, alkaline earth, and transition metal ions are shown in Figures S14–S17 (SI). As may be noted, with the increase of different cations up to 0.5 equiv, the ^{1}MLCT as well as spin-forbidden ^{3}MLCT bands at low energy in the successive absorption curves undergo blue-shifts with the development of new bands in the shorter wavelength region during which they pass through several well-defined isosbestic points.

As there are free >C=O groups in the metal complexes, the possibility of protonation to the oxygen atoms of the free >C=O groups can also be explored. To examine such a possibility, spectrophotometric titrations of the receptors were also carried out with a solution of $HClO_4$ (Figure S18, SI). The spectral changes for the complexes have close resemblance to the spectra of these receptors in the presence of other bivalent cationic guests such as Be^{2+}, Zn^{2+}, etc.

For all metal ions, distinct changes in the absorption spectral profiles of the complexes are observed upon complexation, and clear isosbestic points are found (Figures 10–12 and Figures S11–S18, SI) indicating that only a single equilibrium between two species, namely bimetallic and pentametallic occurs during the titration. Absorption titration profiles of the free bimetallic receptors with various metal ions (insets of Figures 10–12) show a linear increase and a sharp end point at a metal/receptor ratio of 0.5:1, indicating the formation of a $[\mathbf{M^{II}{\cdot}M_1{\cdot}M^{II}}]$ complex (Charts 2 and 3). Due to the lack of curvature in the titration curve, no binding constants can be determined.[61,62] It is of interest to note that on complexation of a metal cation to free >C=O groups of the coordinated dicarboxylate moiety of the metal complexes, blue-shifts of absorption bands occur (Table 5 and Table S5, SI). It may also be noted that the molar extinction coefficients (ε) of the MLCT bands in the resulting pentametallic adducts are much higher (almost double) than those for the free bimetallic hosts (**1** and **2**) as expected. Coordination of a metal

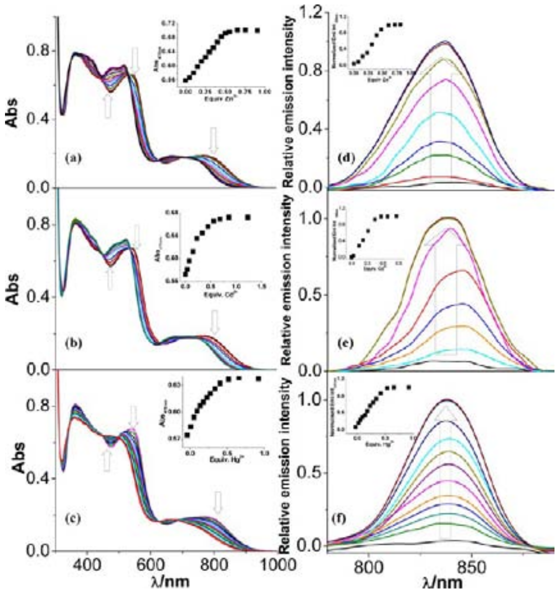

Figure 12. Changes in absorption (a–c) and photoluminescence (d–f) spectra of **2** in acetonitrile solution upon the addition of Zn^{2+}, Cd^{2+}, and Hg^{2+} ion, respectively. Each inset shows the change of absorbance and luminescence intensities as a function of equivalent of metal ion added. The excitation wavelengths are 530, 536, and 503 nm for Zn^{2+}, Cd^{2+}, and Hg^{2+} ion, respectively.

Table 5. Spectroscopic and Photophysical Data of 1 in the Absence and Presence of Various Cations in Acetonitrile Solutions

	absorption	emission		
compds	λ_{max}/nm, ε/M^{-1} cm^{-1}	λ_{max}/nm	$\Phi \times 10^{-3}$	τ/ns
Ru–Ru(**1**)	538 (14697),, 4800 (sh) (9377), 358 (16742)	770	1.15	1.00
1+Zn(II)	500 (29116), 455 (sh) (22666), 355 (34134)	704	8.10	22.89
1+Cd(II)	506 (29194), 461 (sh) (22680), 355 (36004)	710	4.51	21.63
1+Hg(II)	486 (28506), 448 (sh) (23072), 348 (30316)	712	0.78	17.87
1+Cu(II)	487 (28904), 447 (sh) (23168), 349 (31142)	705	0.72	–
1+Ni(II)	494 (29886), 456 (sh) (24458), 352 (36254)	709	0.44	–
1+Co(II)	504 (29402), 460 (sh) (22914), 355 (35354)	705	0.64	–
1+Fe(II)	493 (28754), 455 (sh) (23610), 353 (35078)	708	0.42	–
1+Mn(II)	506 (28424), 459 (sh) (21754), 355 (34952)	708	0.82	–
1+Be(II)	489 (31064), 448 (sh) (25674), 351 (32250)	718	12.25	33.10
1+Mg(II)	511 (31714), 462 (sh) (22472), 355 (38156)	711	8.25	27.26
1+Ca(II)	514 (30038), 463 (sh) (20656), 356 (36890)	704	8.57	19.80
1+Ba(II)	520 (29146), 467 (sh) (19784), 356 (35852)	730	3.40	–
1+$HClO_4$	486 (14738), 444 (sh) (11609), 348 (15648)	709	0.88	–
1+Li(I)	520 (31884), 467 (sh) (20840), 354 (37398)	731	5.32	24.86
1+Na(I)	528 (30216), 470 (sh) (19416), 356 (35402)	750	2.23	22.03
1+K(I)	531 (26454,) 475 (sh) (18194), 356 (32086)	756	1.62	20.28

ion to the host complexes leads to the increase of the net positive charge of the resulting complex backbone, leading to the increase of absorption energies. Although it is clear that the general explanation of a higher energy transition as a function of the more electron-withdrawing metal cation holds for our results, we sought to gain a better understanding of the features of the MLCT bands themselves upon coordination. Computational studies were utilized to help further elucidate the nature of the changes in the absorption manifold upon complexation, vide infra.

Photoluminescence titrations of complexes **1** and **2** with various cations were also carried out in the same way as already described for spectrophotometric measurements. Figures 10 and 11d–f and Figures S11–S13 (SI) show the emission spectral changes of **1** with the addition of incremental amount of different alkali, alkaline earth, and d^{10} transition metal ions to the acetonitrile solution of **1**, and the insets show the change of luminescence intensity vs the equivalents of the cations added. As shown in Figures 10d–f, 11d–e, and S11d–e (SI), the emission maximum at 770 nm gets gradually blue-shifted with consequent enhancement of the luminescence intensity with increasing cation concentration in all cases with the exception of Ca^{2+} and Hg^{2+} ions (Figure 11f and Figure S11f [SI], respectively), where little quenching of the luminescence intensity occurs with incremental addition of the said ions. The results indicate that on coordination of selective cationic guests (with the exception of Ca^{2+} and Hg^{2+} ions) to the free bimetallic hosts (**1** and **2**), an increase in energy of the excited state and enhancement of the radiative decay of the adducts occur. Insets to Figures 10, 11d–f, and S11d–f (SI) indicate that intensity of the emission band becomes maximized when the host-to-cation guest ratio reaches 1:0.5. Photoluminescence titrations of the receptor **1** with different paramagnetic 3d bivalent metal cations (Mn^{2+}, Fe^{2+}, Co^{2+}, Ni^{2+}, and Cu^{2+}) were also investigated, and Figures S12d–f and S13c,d (SI) show the quenching of emission intensity of the receptor on incremental addition of metal cations. In contrast to alkali, alkaline earth, and d^{10} transition metal ions, nearly complete quenching of emission at 770 nm for free **1** is observed following the addition of about 0.5 equiv of each of these ions.

The photophysical behavior of the osmium(II) compound (**2**) turns out to be highly interesting because, despite the fact that it does not exhibit photoluminescence in acetonitrile at room temperature, in the presence of certain cationic guests it exhibits luminescence. The onset of the emission band around the 800–850 nm region with the addition of Be^{2+}, Mg^{2+}, or Ca^{2+} as well as Zn^{2+}, Cd^{2+}, or Hg^{2+} ions to an acetonitrile solution of **2** is shown in Figure S15d–f (SI) and Figure 12d–f. Insets to Figure S15d–f (SI) and 12d–f indicate that the intensity of the emission band becomes maximized when the host-to-cation guest ratio reaches 1:0.5. On the other hand no emission is observed for **2** with the alkali metals as well as with paramagnetic bivalent transition metal ions such as Mn^{2+}, Fe^{2+}, Co^{2+}, and Ni^{2+}.

It is of interest to note that the complex **1** acted as an "off–on" emission switch with selective alkali, alkaline earth, and d^{10} transition metal ions, while in the presence of Mn^{2+}, Fe^{2+}, Co^{2+}, Ni^{2+}, or Cu^{2+} the same complex acted as "on–off" emission switch. Complex **2** on the other hand acted only as an "off–on" emission switch with selective cations. Figure 13 shows the time-resolved decay profiles of the receptor **1** as functions of different alkali, alkaline earth, and d^{10} transition metal ions. In the presence of the metal ions, luminescence decays double exponentially with a short component having a decay constant comparable to the

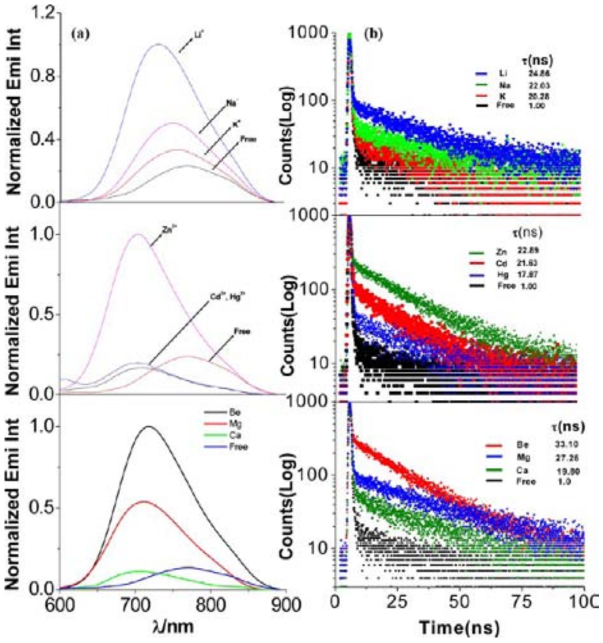

Figure 13. Changes in (a) steady-state emission spectra and (b) time-resolved fluorescence decay profiles of **1** in acetonitrile at room temperature upon addition of different cationic guests.

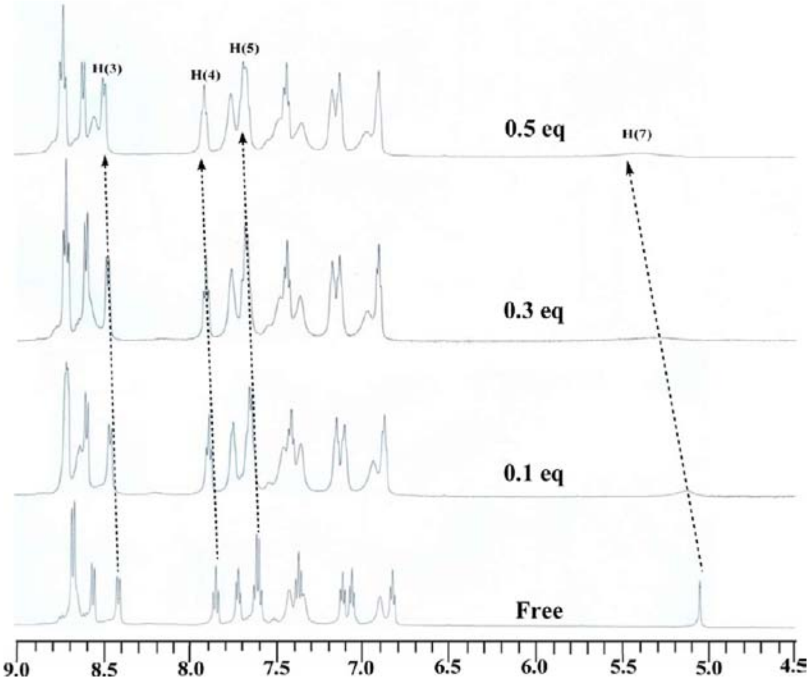

Figure 14. ^{1}H NMR (500 MHz) titration of **2** in DMSO-d_6 solution (5.0×10^{-3} M) upon addition of Li^+ ion (1.2×10^{-1} M, 0–0.5 equiv).

lamp profile and a long component with a lifetime which gradually increases as we go upward in a particular group of alkali, alkaline earth, or d^{10} transition metal ions. These data suggest that, on addition of selective metal ions to the solution of free receptor **1**, formation of metal-bridged species (pentameric, [**1**·$\mathbf{M_1}$·**1**]) occur, and the lifetimes of the resulting species become longer than that of the free receptor, and the net result is the observed lifetime enhancement as shown in Figure 13. The luminescence intensities of Ru^{II} and Os^{II} polypyridine complexes typically originate from the lowest ^{3}MLCT excited state because of the large spin–orbit coupling exerted by Ru^{II} or Os^{II}, and their decay follows the energy gap law where the nonradiative decay process becomes more efficient when the energy gap between the ground state and the emissive excited state is smaller because of the greater vibrational overlap with the two electronic states.[1] In our cases, the luminescence intensities as well as lifetimes of the metal-bridged species are longer than those of the parent bimetallic host complexes. On coordination of a cationic guest to the bimetallic host, formation of the pentameric species occurs, and it is highly probable that in the pentameric complexes the energy gap between the emitting ^{3}MLCT state and thermally activated ^{3}MC state increases, thereby enhancing the luminescence intensities as well as luminescence lifetimes.

Coordination of the metal ions such as Mn^{2+}, Co^{2+}, or Cu^{2+} triggers the emission quenching of the receptor **1**, while the metal ions having a completely filled d orbital (such as Zn^{2+}, Cd^{2+}, or Hg^{2+}) do not quench; rather some finite enhancement of the emission intensity of the receptor occurs. This observation is probably due to the photoinduced electron transfer (PET) mechanism, which goes via an excited-state electron transfer process as shown below.[63,64] The present bimetallic host complexes can be considered as a combination of fluorophore/receptor, where the M(bpy)$_2$ units are the fluorophores and two CO units arranged in a bidentate fashion in the complex are receptors which can coordinate to cationic guests. The 3d series transition metal ions having incompletely filled d orbitals can drag the electron after excitation and can go to lower oxidation state(s). Emission quenching of **1** in the presence of Fe^{2+}, Co^{2+}, Ni^{2+}, or Cu^{2+} could also be due to the energy transfer from the emitting ^{3}MLCT excited state to the low-lying thermally activated low-lying metal-centered dd state.

$$[\{M^{II}(Imdc)M^{II}\}^{*}\text{—}Cu^{II}] \rightarrow [\{M^{III}(Imdc)M^{II}\}^{*}\text{—}Cu^{I}](M = \text{Ru or Os})$$

On the other hand, in the case of the Zn^{2+}, Cd^{2+}, or Hg^{2+}, the nonavailability of the variable oxidation states as well as the fact that it has a stable d^{10} electronic configuration does not consume the electron. Hence, PET does not occur, and the fluorescence of the receptor is not quenched in the presence of Zn^{2+}, Cd^{2+}, or Hg^{2+}.

Again it is of interest to assess relative efficacies of complexes as hosts to accommodate a particular metal ion as a guest and also to find to what extent the affinities of the guest cations (such as Li^+, Na^+, and K^+) differ for a particular host complex. By comparing the extent of changes in the absorption and emission spectral measurements, it may be concluded that among the three guest alkali metals, the decreased order of their binding with both host complexes is $Li^+ > Na^+ > K^+$. Again among the three guest alkaline earth metals, the decreased order of their binding with both host complexes is $Be^{2+} > Mg^{2+} > Ca^{2+}$. The size and charge of the guest cation turns out to be important for binding the host metal complexes. Thus, the increased order of the ionic radii of the guest cation appears to be correlated with their binding capacities.

To prove the interaction of metalloreceptors with various cations, ^{1}H NMR titrations were carried out with increasing amounts of cations added to DMSO-d_6 solutions of the complexes **1** and **2**. Typically a 5.0×10^{-3} M solution of **2** in DMSO-d_6 was titrated with Li^+ ion up to 1 equiv. Figure 14 shows that the imidazole C–H proton of coordinated $Imdc^{3-}$ appeared as a singlet in a profoundly upfield region (5.03 ppm) as a consequence of the increase in electron density of the imidazole

Table 6. Selected UV–Vis Energy Transitions at the TD-DFT/B3LYP Level for **1**, [**1**·H], [**1**·Li], and [**1**·Li·**1**] in Acetonitrile

excited state	λ_{cal}/nm /ε_{cal}/ M^{-1} cm^{-1}/(eV)	oscillator strength (f)	λ_{expt}/nm /ε_{expt}/ M^{-1} cm^{-1}/(eV)	key transitions	character
1 (peak width at half-maximum =0.17 eV)					
S_{7}	534(14573), 2.32	0.21	538(14697), 2.30	H-4→L+1(27%), H-3→L (22%), H-1→LUMO(10%)	MLLCT
S_{12}	475 (8183), 2.61	0.06	482 (9377), 2.57	H-4→L+3(21%), H-3→L+2(27%), H-1→L+2(17%)	MLLCT
S_{39}	362(25866), 3.49	0.17	358(16742), 3.46	H-3→L+6(14%), H-1→L+8(15%), H→L+9(26%),	MLCT
S_{114}	277(102553), 4.47	0.37	294(75313), 4.21	H-12→L+2(12%), H-10→L+2(13%), H-9→L+3(11%),	$\pi-\pi^*$/ILCT
S_{196}	240 (22790), 5.16	0.12	245(40935), 5.06	H-12→L+4(11%), H-11→L+5(10%), H-16→L+2(7%), H-15→L+3(7%) H-7→L+12(7%), H-6→L+12(8%) H-4→L+20(7%)	$\pi\pi^*$
[**1**·H] (peak width at half-maximum =0.14 eV)					
S_{6}	488(14799), 2.54	0.14	486(14738), 2.55	H-2→L+1(36%), H-2→L+3(28%), H-1→L+3(20%)	MLCT
S_{11}	439(11245), 2.82	0.09	444(11609), 2.79	H-3→L+3(12%), H-2→L+3(38%), H-1→L+3(14%)	MLCT
S_{44}	339(18388), 3.65	0.09	348(15648), 3.56	H-2→L+8(18%), H-1→L+8(16%), H→L+11(14%), H→L+12(19%)	MLCT/ $\pi-\pi^*$
S_{103}	275(116593), 4.50	1.19	290(82063), 4.27	H-10→L (12%), H-9→L+2(20%), H-8→L+1(15%),H-7→L+3(22%)	$\pi-\pi^*$/ILCT
S_{180}	238(25495), 5.23	0.03	245(35672), 5.06	H-12→L+1(20%), H-12→L+3(47%)	$\pi-\pi^*$
[**1**·**Li**] (peak width at half-maximum =0.15 eV)					
S_{10}	490(14844), 2.53	0.22	–	H-4→L+1(23%), H-3→L (14%), H-2→L+3(12%), H-1→L(15%)	MLCT
S_{11}	462(12681), 2.68	0.11	–	H-4→L+3(20%), H-3→L+2(17%), H-1→L+2(26%)	MLCT
S_{44}	356(17646), 3.48	0.10	–	H-3→L+7(21%), H-2→L+8(13%), H→L+9(23%)	MLCT/ $\pi-\pi^*$
S_{44}	278(83904), 4.48	0.12	–	H-10→L (10%), H-9→L+1(14%), H-8→L+2(27%),H-7→L+3(25%)	$\pi-\pi^*$/ILCT
S_{44}	241(21209), 5.27	0.10	–	H-14→L+2(21%), H-8→L+7(8%), H-8→L+12(8%), H-7→L+8(6%), H-7→L+11(8%), H-5→L+14 (7%)	$\pi-\pi^*$
[**1**·**Li**·**1**] (peak width at half-maximum = 0.17 eV)					
S_{16}	516(32798), 2.40	0.39	520(31884), 2.38	H-9→L+1(6%), H-8→L+2(5%), H-7→L+3(6%), H-2→L+3(6%), H-6→L+2(4%), H-4→L+6 (4%), H-3→L+2(4%),H-1→L+6 (4%),	MLCT
S_{18}	488(31360), 2.54	0.12	467(20840), 2.65	H-8→L+3(8%), H-6→L+1(6%), H-2→L+1(6%), H-1→L+5(5%), H-9→L (4%), H-9→L+1(4%), H-9→L+2(4%), H-7→L+2(4%)	MLCT
S_{128}	355(44350), 3.49	0.23	354(37398), 3.50	H-1→L+19(9%), H-7→L+13(6%), H-6→L+14(6%), H-7→L+14(4%), H-4→L+15(4%), H-2→L+25(4%), H-1→L+23(4%), H→L+18(4%)	MLCT/ $\pi-\pi^*$

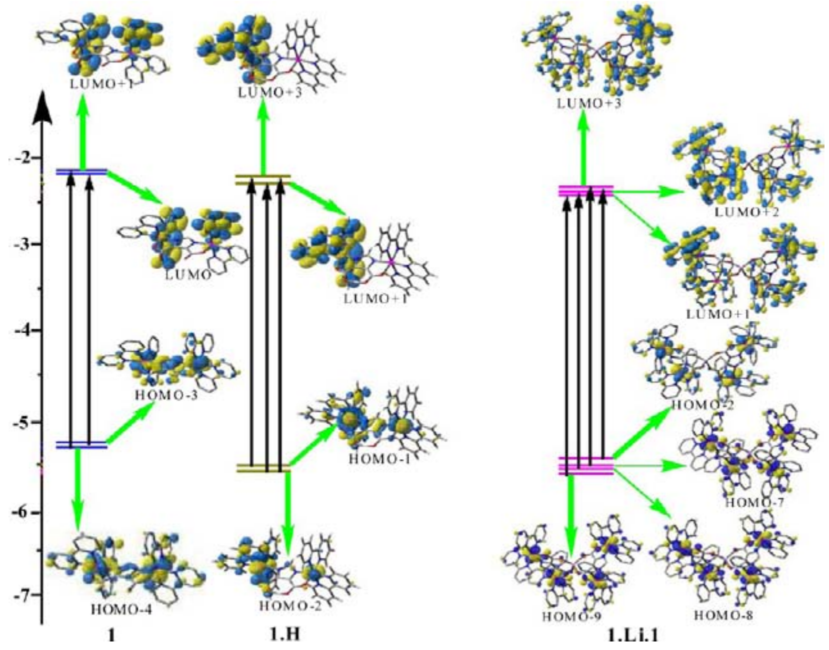

Figure 15. Energy level diagrams depicting the dominant transitions that comprise the lowest-energy absorption band for **1**, [**1**·H], and [**1**·Li·**1**].

moiety due to the deprotonation of the N−H and two COOH protons and subsequent delocalization of the net negative charge throughout the $Imdc^{3-}$ moiety. It is interesting to note that the chemical shift of the imidazole C−H proton gets progressively downfield-shifted along with subsequent broadening on gradual addition of Li^+ ion up to 0.5 equiv. Further addition of Li^+ ion beyond 0.5 equiv to the solution of **2** does not lead to any change in the ^1H NMR spectrum, indicating the formation of the pentametallic ([**2·Li·2**]) species. It may be mentioned that the formation of the pentametallic species was also confirmed by absorption and emission titration experiments. Bipyridine protons (H4−H6), on the other hand, are far less affected upon addition of Li^+ ion. As expected, a small but finite downfield-shift occurs for the bpy protons on titration with metal ion. A similar behavior was also observed with **1** (Figure S19, SI). Thus, the results of the titration experiment clearly indicate the net drainage of electron density from the imidazole-dicarboxylate ($Imdc^{3-}$) moiety in **1** and **2** on coordination with the cationic guest.

In order to check the mode of interaction of the receptors with metal ions, IR spectra of free **1** and **2** and in presence of 0.5 and 1.0 equiv of metal ions were also recorded. IR spectra of **1** and **2** in absence and in presence of 0.5 equiv of Li^+ ion are shown in Figures S20−S21 (SI). The signal due to carboxylate stretching frequency (ν_{CO}) appears at 1610 cm^{-1} for **1** and 1632 cm^{-1} for **2** in their IR spectra. In both cases, distinct changes in the ν_{CO} frequencies occur in the presence of the added metal ion, indicating the formation of adduct with the incoming cationic guest through the free >C═O groups in the already coordinatively saturated host complexes **1** and **2**. It may also be mentioned that the spectrum recorded in the presence of 0.5 equiv of Li^+ ion is almost the same as that recorded in the presence of 1.0 equiv of the metal ion (not shown in Figures S20−S21, SI).

Singlet Excited States and Calculated Absorption Spectra. In order to understand the nature of the underlying excited states involved in the experimental absorption spectra, theoretical calculations are essential. With the prerequisite ground-state DFT calculation in hand, we proceed to compute the UV−vis spectra of both the complexes as well as protonated ([**1·H**] and [**2·H**]) and lithiated adducts ([**1·Li·1**] and [**2·Li·2**]) of the complexes in solution using a TD-DFT approach. The energy of each excited state is the vertical excitation energy in electron volts (eV) from the ground state. The calculated absorption energies associated with their oscillator strengths, the main configurations, and their assignments are given in Tables 6 and S6 (SI). Figures 15 and S22 (SI) display the energy levels of different molecular orbitals involved in the electronic transition process of the complexes. Figure 16 presents combined experimental and simulated UV−vis spectra of the complexes (**1**, [**1·H**], [**1·Li·1**], and **2**, [**2·H**], [**2·Li·2**]), while the simulated UV−vis spectrum of lithiated trimeric complex [**1·Li**] are shown in Figure S23 (SI).

The calculated lowest-energy absorption band in the visible region is obtained at 534 nm with oscillator strength 0.21 for **1** and 527 nm with oscillator strength 0.19 for **2**. Of all the possible vertical excitations, the excitation of HOMO−4 → LUMO+1 (27%), HOMO−3 → LUMO (22%), and HOMO−1 → LUMO (10%) mainly contribute to the absorption band around 534 nm for **1**. On the other hand, HOMO−5 → LUMO (16%), HOMO−4 → LUMO+1 (21%), HOMO−2 → LUMO+3 (10%), HOMO−1 → LUMO+1 (17%), and HOMO → LUMO +3 (12%) mainly contribute to the absorption band around 527 nm for **2**. As reported in Table S3 (SI), the occupied molecular orbitals (H−H-3) are mainly localized on Ru or Os metal (67.8−78.3%) with some contribution from bpy (10.9−20.6%) and $Imdc^{3-}$ ligand (8.7−12.7%). While the virtual molecular orbital (L−L+3) are predominantly composed of bpy ligand with the composition of 86.8−93.7%. Thus, the transitions are effectively metal (Ru or Os)-ligand (bpy and/or $Imdc^{3-}$) to ligand (bpy) charge transfer (MLLCT) transitions. The next higher energy absorption (shoulder) in the visible appears at 475 nm (f = 0.06) for **1** and at 432 nm (f = 0.07) nm for **2**. Again, on the basis of the frontier molecular orbital (FMO) composition data in Table S3 (SI), the MLCT transitions can be assigned as the charge transfer from metal (Ru or Os)-ligand (bpy and/or $Imdc^{3-}$) to ligand (bpy) charge transfer (MLLCT) transitions. There are three additional bands predicted at 362, 277, and 240 nm for **1**, while 364, 275, and 239 nm for **2** in acetonitrile and the assignments of these transitions are given in Table 6 and Table S6 (SI).

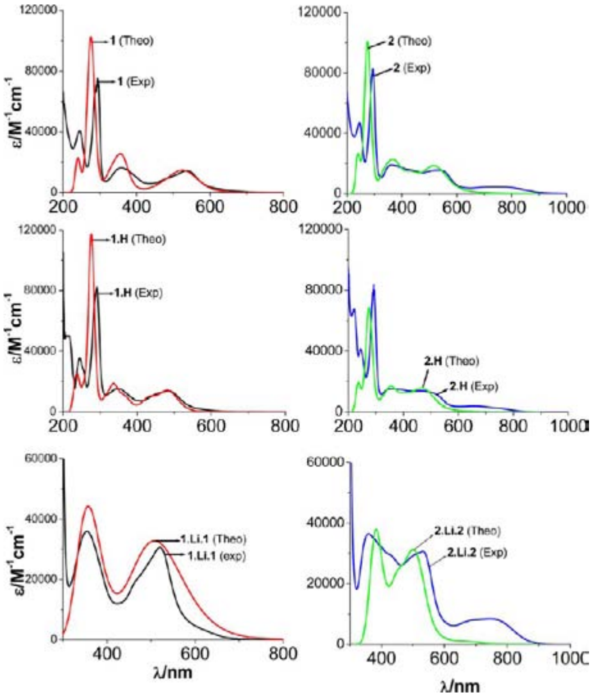

Figure 16. Experimental and calculated absorption spectra of **1**, **2**, [**1·H**], [**2·H**], [**1·Li·1**] and [**2·Li·2**] in acetonitrile at room temperature.

We have also computed the UV−vis spectra of the protonated ([**1·H**] and [**2·H**]) as well as pentameric complexes ([**1·Li·1**] and [**2·Li·2**]) of Ru and Os in the solution (acetonitrile) phase using TD-DFT approach. The calculated absorption energies associated with their oscillator strengths, the main configurations, and their assignments are already given in Table 6 and Table S6 (SI). Figure 16 already presented the combined experimental and simulated UV−vis spectra of the complexes.

A comparison of experimental and calculated absorption spectral data for **1** and **2** in acetonitrile is given in Table 6 and Table S6 (SI). It shows that the computed data are in agreement with the experimental data for both band positions and relative intensity. We observe a variation of 1−24 nm for all the absorption bands. Such differences are within the typical accuracy of TD-DFT calculations for MLCT excitations in transition metal complexes.[44−58] The effect of protonation or coordination of a cationic guest to the bimetallc host complexes (**1** and **2**) is also evidenced from our calculations. In particular, experimentally observed blue-shift of the low-energy MLCT

Table 7. Phosphorescence Emission of the Complexes in Acetonitrile Solution According to TD-DFT and UKS Calculations and Associated Experimental Value

compounds	transition	key transitions	TD-DFT λ/nm	UKS λ/nm	exptl. λ/nm	assignment
1	$^3A' \to ^1A'$	LUMO→HOMO (87%), LUMO→HOMO-4(4%)	859	739	770	MLCT
[**1·H**]	$^3A' \to ^1A'$	LUMO→HOMO (85%), LUMO→H-1(5%)	745	697	708	MLCT
[**1·Li**]	$^3A' \to ^1A'$	LUMO→HOMO (65%), LUMO→H-1(16%)	792	701	–	MLCT
[**1·Li·1**]	$^3A' \to ^1A'$	L+4→H-3 (20%), L+4→H-2(15%)	828	709	731	MLCT

bands when going from bimetallic to its corresponding protonated ([**1·H**] and [**2·H**]) or pentametallic ([**1·Li·1**] and [**2·Li·2**]) form are well reproduced in our TD-DFT calculations (Table 6 and Table S6, SI).

The Os complexes experimentally show an additional weak and broad absorption band at longer wavelength (600−700 nm). This lower energy transitions has been supposed to be an electronic transition between the ground and the triplet excited state of the Os compounds, allowed by spin−orbit coupling.[1,5] Since singlet−triplet mixing was not taken into account in our calculations, it is thus not possible from our results to determine what effect these triplet states have on the ground-state absorption spectrum of the Os(II) complexes.

Geometries in the Lowest-Lying Triplet Excited State and Calculated Emission Spectra. The lowest triplet states, T_1 of **1**, [**1·H**], [**1·Li**], and [**1·Li·1**] have also been optimized in the solution state by using TD-DFT methodology and selected geometrical parameters are already given in Table 3 and their optimized structures are depicted in Figure S24 (SI). In addition to TD-DFT, UKS calculations were also performed directly on the triplet state of the complexes and their few selected adducts. The calculated results indicate that geometrical parameters of complexes in the triplet states have small differences from their ground-state structures.

The emission energies of complexes **1** and **2** and the above-mentioned adducts in acetonitrile medium were calculated from the energy difference between the ground singlet and the excited lowest triplet state in the optimized geometry. The S_0/T_1 vertical gaps are reported in Table 7 and Table S7 (SI). The plots of frontier molecular orbitals related to emissions of **1**, [**1·H**], [**1·Li**], and [**1·Li·1**] are presented in Figure 17, while those of **2**, [**2·H**], and [**2·Li·2**] are shown in Figure S25 (SI). According to TD-DFT calculations, the lowest-energy emissions were obtained at 859, 745, 792, and 828 nm for **1**, [**1·H**], [**1·Li**], and [**1·Li·1**], respectively, in acetonitrile solution (Table 7). On the other hand, the calculated values of emission maxima on the basis of UKS calculations are 739, 697, 701, and 709 nm, for **1**, [**1·H**], [**1·Li**], and [**1·Li·1**], respectively.

In order to discuss the nature of the emission, we present the compositions of the frontier MOs of **1**, [**1·H**], [**1·Li**], and [**1·Li·1**] in Table 8. It is seen from the table that the HOMOs are composed mainly of Ru^{II} (71.7−79.8%) with some minor contributions from $Imdc^{3-}$ (0.05−11.9%) as well bipyridine (12.5−17.9%) ligands, whereas the LUMOs are predominantly localized on the bipyridine fragment. Calculations also reveal that, among all the possible transitions, LUMO → HOMO (87%) and HOMO−4 (4%) mainly contribute to the emission for **1**, LUMO → HOMO (85%) and HOMO−1 (5%) for [**1·H**], LUMO → HOMO (65%) and HOMO−1 (16%) for [**1·Li**], and LUMO+4 → HOMO−3 (20%) and HOMO−2 (15%) for [**1·Li·1**]. Thus, the calculated emissions at 739, 697, 701, and 709 nm for **1**, [**1·H**], [**1·Li**], and [**1·Li·1**], respectively, can be assigned as the transitions from predominantly ^{3}MLCT states. Previously, we observed that the experimental emissions were obtained at 770, 708, and 731 nm for **1**, [**1·H**], and [**1·Li·1**], respectively, which correspond to the respective calculated values of 739, 697, and 709 nm (based on UKS). Thus, the experimentally observed emissions at 770, 708, and 731 nm for **1**, [**1·H**], and [**1·Li·1**], respectively, can be assigned as the transitions from ^{3}MLCT levels. Moreover, the trends of the experimentally observed blue-shifts of emission maxima on going from **1** to [**1·H**] (708 nm) or [**1·Li·1**] (731 nm) can also be reproduced by the calculated results. It is to be noted from Table 7 that, as compared with TD-DFT approach, the calculated values of emission maxima of the complexes obtained by the UKS method are closer to those of the experimentally observed values. It may be mentioned that Os(II) complex **2** does not show any luminescence at room temperature. Because the emissive ^{3}MLCT is lower in energy for the Os(II) complex (Table S7, SI), nonradiative decay to the ground state should be more

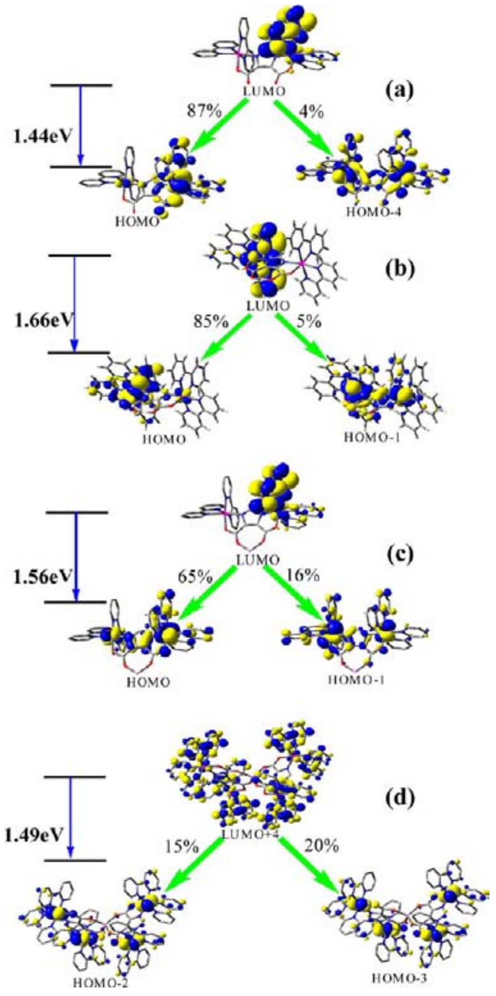

Figure 17. Calculated single-electron transitions for the emissions of T_1 states for **1** (a), [**1·H**] (b), [**1·Li**] (c), and [**1·Li·1**] (d).

Table 8. Compositions of Partial Frontier MOs of 1, [1·H], [1·Li], and [1·Li·1] in Acetonitrile in the Lowest-Lying $^3A'$ Excited States

	energy/eV		composition/%		
MO		Ru^{II}	Li^{I}[a]	$Imdc^{3-}$[a]	bpy
	1				
HOMO−4	−5.454	72.8	–	10.3	16.9
HOMO	−5.129	74.2	–	11.9	13.9
LUMO	−2.479	10.3	–	1.2	88.5
	[1·H]				
HOMO−1	−5.701	77.4	–	10.1	12.5
HOMO	−5.542	77.8	–	6.9	15.2
LUMO	−2.665	9.1	–	1.5	89.4
	[1·Li]				
HOMO−1	−5.672	0.01	8.5	17.9	
HOMO	−5.595	71.7	0.00	10.6	17.6
LUMO	−2.831	6.7	0.02	1.3	92.0
	[1·Li·1]				
HOMO−3	−5.555	9.3	0.05	12.8	
HOMO−2	−5.472	79.8	6.3	0.05	13.9
LUMO+4	−2.346	6.7	0.7	0.28	92.3

[a] As the contribution of Li^+ ion and $Imdc^{3-}$ in [**1·Li**] and [**1·Li·1**] are very small, 2 decimal digits were given.

efficient. However, the protonated as well as some pentametallic adducts of **2** show moderately strong luminescence at room temperature. It is highly probable that, in the protonated as well as pentameric adducts, the energy gap between the emitting MLCT state and thermally activated dd state increases, thereby enhancing the luminescence.

CONCLUSIONS

We are interested in studying molecular systems whereby the photophysical and photochemical properties can be readily tuned by adding selective cationic guests, through experimental and computational means. In this context, we have presented combined experimental and theoretical studies of two mixed-ligand bimetallic ruthenium(II) and osmium(II) complexes of composition, $[(bpy)_2M(Imdc)M(bpy)_2]^+$ [M = Ru^{II} (**1**) and M = Os^{II} (**2**)], where H_3Imdc = imidazole-4,5-dicarboxylic acid and bpy = 2,2′-bipyridine. On the experimental side, single-crystal X-ray structures of both the complexes were determined. The effects of alkali, alkaline earth, and transition metal cations on the absorption and emission spectral behavior of the complexes have been studied in detail. As compared to the free complexes, the luminescence intensities and the quantum yields of the complexes are enhanced substantially in the presence of selective cations showing cation-induced molecular switching behaviors in the complexes.

To gain a better understanding of the electronic structure and excited-state properties, we have also carried out density functional theory (DFT) and time-dependent DFT (TD-DFT) calculations of the complexes in gas as well as solution phase. There is an overall satisfactory agreement between the optimized geometrical parameters for the complexes computed both in the gas phase and in solution and the experimental X-ray data. The good agreement between the experimental and the TD-DFT calculated absorption spectra of the complexes allowed us to provide a detailed assignment of the main spectral features of the investigated complexes. In particular, the blue-shifts of the absorption and emission bands of the host complexes in the presence of selective cations as well as protons are also reproduced by our calculations. Moreover, the emitting properties of the osmium(II) compound turns out to be highly interesting because, despite the fact that it does not exhibit photoluminescence in acetonitrile at room temperature, in the presence of certain cationic guests it exhibits luminescence in the near-infrared region. This may open the possibility of the application of such compounds as cation-driven molecular switches, particularly in the near-infrared region.

ASSOCIATED CONTENT

Supporting Information

X-ray crystallographic data for complexes **1** and **2** in CIF format. Calculated bond distances and angles, MOs along with their energies and compositions, spectroscopic and photophysical data, UV−vis energy transitions at the TD-DFT/B3LYP level, phosphorescence emission of the complexes, mass and COSY spectra, optimized geometries, schematic drawings of FMOs, CV, and SWV, absorption, emission, ^1H NMR, and IR spectral changes of **1** and **2** upon the addition of cations, energy level diagrams, etc. This material is available free of charge via the Internet at http://pubs.acs.org.

AUTHOR INFORMATION

Corresponding Author

*E-mail: sbaitalik@hotmail.com

Notes

The authors declare no competing financial interest.

ACKNOWLEDGMENTS

We thank Dr. Ajay Kumar Mishra of the Department of Chemistry and Chemical Technology of Vidyasagar University for his valuable input in the area of DFT and TD-DFT computation. Financial assistance received from the Department of Science and Technology, New Delhi [Grant No. SR/S1/IC-33/2010] is gratefully acknowledged. Thanks are due to the DST for providing the single-crystal X-ray diffractometer in FIST and time-resolved nanosecond spectrofluorimeter in PURSE Programme at Department of Chemistry of Jadavpur University. S.D. and S.K. thank CSIR for their fellowship.

REFERENCES

(1) (a) Juris, A.; Balzani, V.; Barigelletti, F.; Campagna, S.; Belser, P.; von Zelewsky, A. *Coord. Chem. Rev.* **1988**, *84*, 85. (b) Balzani, V.; Juris, A.; Venturi, M.; Campagna, S.; Serroni, S. *Chem. Rev.* **1996**, *96*, 759. (c) Campagna, S.; Puntoriero, F.; Nastasi, F.; Bergamini, G.; Balzani, V. *Top. Curr. Chem.* **2007**, *280*, 117−214. (d) Meyer, T. J. *Pure Appl. Chem.* **1986**, *58*, 1193. (e) Sun, L.; Hammarström, L.; Akermark, B. *Chem. Soc. Rev.* **2001**, *30*, 36.

(2) (a) Balzani, V.; Credi, A.; Venturi, M. *Molecular Devices and Machines*; Wiley-VCH: Weinheim, 2003. (b) Wang, X.; Guerzo, A.; Baitalik, S.; Simon, G.; Shaw, G. B.; Chen, L. X.; Schmehl, R. *Photosynth. Res.* **2006**, *87*, 83. (c) Baitalik, S.; Wang, X.; Schmehl, R. H. *J. Am. Chem. Soc.* **2004**, *126*, 16304. (d) Browne, W. R.; O'Boyle, N. M.; McGarvey, J. J.; Vos, J. G. *Chem. Soc. Rev.* **2005**, *34*, 641. (e) Medlycott, E. A.; Hanan, G. S. *Coord. Chem. Rev.* **2006**, *250*, 1763. (f) Medlycott, E. A.; Hanan, G. S. *Chem. Soc. Rev.* **2005**, *34*, 133. (g) Kuang, D.; Ito, S.; Wenger, B.; Klein, C.; Moser, J.-E.; Humphry-Baker, R.; Zakeeruddin, S. M.; Gratzel, M. *J. Am. Chem. Soc.* **2006**, *128*, 4146. (h) Barton, J. K. *Science* **1986**, *233*, 727. (i) Kozlov, D. V.; Tyson, D. S.; Goze, C.; Ziessel, R.; Castellano, F. N. *Inorg. Chem.* **2004**, *43*, 6083. (j) Ji, S.; Wu, W.; Wu, W.; Song, P.; Han, K.; Wang, Z.; Liu, S.; Guo, H.; Zhao, J. *J. Mater. Chem.* **2010**, *20*, 1953. (k) Abrahamsson, M.; Jäger, M.; Kumar, R. J.; Österman, T.; Persson, P.; Becker, H.-C.; Johansson, O.; Hammarström, L. *J. Am. Chem. Soc.* **2008**, *130*, 15533 and references therein.

(3) (a) Zhao, Q.; Huanga, C.; Li, F. *Chem. Soc. Rev.* **2011**, *40*, 2508. (b) Fabian, J.; Makazumi, H.; Matsuoka, M. *Chem. Rev.* **1992**, *92*, 1197. (c) Qian, G.; Wang, Z. Y. *Chem. Asian J.* **2010**, *5*, 1006. (d) Fernandez-Moreira, V.; Thorp-Greenwood, F. L.; Coogan, M. P. *Chem. Commun.* **2010**, *46*, 186.

(4) (a) Wu, S.-H.; Burkhardt, S. E.; Yao, J.; Zhong, Y.-W.; Abruña, H. D. *Inorg. Chem.* **2011**, *50*, 3959. (b) Elmes, R. B. P.; Orange, K. N.; Cloonan, S. M.; Williams, D. C.; Gunnlaugsson, T. *J. Am. Chem. Soc.* **2011**, *133*, 15862. (c) Elmer, R. B. P.; Kitchen, J. A.; Williams, D. C.; Gunnlaugsson, T. *Dalton Trans.* **2012**, *41*, 6607. (d) Ward, M. D.; McCleverty, J. A. *J. Chem. Soc., Dalton Trans.* **2002**, 275. (e) Chen, J.-L.; Chi, Y.; Chen, K.; Cheng, Y.-M.; Chung, M.-W.; Yu, Y.-C.; Lee, G.-H.; Chou, P.-T.; Shu, C.-F. *Inorg. Chem.* **2010**, *49*, 823. (f) Treadway, J. A.; Strouse, G. F.; Ruminski, R. R.; Meyer, T. J. *Inorg. Chem.* **2001**, *40*, 4508.

(5) (a) Schubert, U. S.; Eschbaumer, C. *Angew. Chem., Int. Ed.* **2002**, *41*, 2892. (b) Harriman, A.; Ziessel, R. *Chem. Commun.* **1996**, 1707. (c) Barigelletti, F.; Flamigni, L. *Chem. Soc. Rev.* **2000**, *29*, 1. (d) Ziessel, R. *Synthesis* **1999**, 1839. (e) Balzani, V.; Juris, A. *Coord. Chem. Rev.* **2001**, *211*, 97. (f) Eryazici, I.; Moorefield, C. N.; Newkome, G. R. *Chem. Rev.* **2008**, *108*, 1834. (g) Constable, E. C. *Chem. Soc. Rev.* **2007**, *36*, 246. (h) Baranoff, E.; Collin, J.-P.; Flamigni, L.; Sauvage, J.-P. *Chem. Soc. Rev.* **2004**, *33*, 147.

(6) (a) Lehn, J.-M. *Supramolecular Chemistry, Concepts and Perspective*; VCH: Weinheim, Germany, 1995. (b) de Silva, A. P.; Gunaratne, H. Q. N.; Gunnlaugsson, T.; Huxley, A. J. M.; McCoy, C. P.; Rademacher, J. T.; Rice, T. E. *Chem. Rev.* **1997**, *97*, 1515.

(7) Sessile, J. L.; Gale, P. A.; Cho, W. S. *Anion Receptor Chemistry*; Royal Society of Chemistry: Cambridge, U.K., 2006.

(8) (a) Nolan, E. M.; Lippard, S. J. *Chem. Rev.* **2008**, *108*, 3443. (b) Czarnik, A. *Fluorescent Chemosensors for Ion and Molecule Recognition*, W. Ed. American Chemical Society, Washington, D.C., 1992; (c) Domaille, D. W.; Que, E. L.; Chang, C. J. *Nat. Chem. Biol.* **2008**, *4*, 168. (d) Kim, H. M.; Cho, B. R. *Acc. Chem. Res.* **2009**, *42*, 863. (e) Xu, Z.; Yoon, J.; Spring, D. R. *Chem. Soc. Rev.* **2010**, *39*, 1996.

(9) (a) Saha, S.; Stoddart, J. F. *Chem. Soc. Rev.* **2007**, *36*, 77. (b) Gan, Q.; Ferrand, Y.; Bao, C.; Kauffmann, B.; Grélard, A.; Jiang, H.; Huc, I. *Science* **2011**, *331*, 1172. (c) Belevich, I.; Verkhovsky, M. I.; Wilkström, M. *Nature* **2006**, *440*, 829. (d) Huynh, M. H. V.; Meyer, T. J. *Chem. Rev.* **2007**, *107*, 5004. (e) Haga, M.; Ali, M. M.; Maegawa, H.; Nozaki, K.; Yoshimura, A.; Ohno, T. *Coord. Chem. Rev.* **1994**, *132*, 99. (f) Manner, V. W.; Mayer, J. M. *J. Am. Chem. Soc.* **2009**, *131*, 9874. (g) Browne, W. R.; O'Boyle, N. M.; Henry, W.; Guckian, A. L.; Horn, S.; Fett, T.; O'Connor, C. M.; Duati, M.; De Cola, L.; Coates, C. G.; Ronayne, K. L.; McGarvey, J. J.; Vos, J. G. *J. Am. Chem. Soc.* **2005**, *127*, 1229.

(10) (a) Saha, D.; Das, S.; Bhaumik, C.; Dutta, S.; Baitalik, S. *Inorg. Chem.* **2010**, *49*, 2334. (b) Bhaumik, C.; Das, S.; Saha, D.; Dutta, S.; Baitalik, S. *Inorg. Chem.* **2010**, *49*, 5049. (c) Saha, D.; Das, S.; Maity, D.; Dutta, S.; Baitalik, S. *Inorg. Chem.* **2011**, *50*, 46. (d) Bhaumik, C.; Saha, D.; Das, S.; Baitalik, S. *Inorg. Chem.* **2011**, *50*, 12586. (e) Das, S.; Saha, D.; Bhaumik, C.; Dutta, S.; Baitalik, S. *Dalton Trans.* **2010**, *39*, 4162.

(11) (a) Martínez-Máñez, R.; Sancenón, F. *Chem. Rev.* **2003**, *103*, 4419. (b) Beer, P. D. *Coord. Chem. Rev.* **2000**, *205*, 131. (c) Sun, S.-S.; Lees, A. J. *Coord. Chem. Rev.* **2002**, *230*, 171. (d) Suksai, C.; Tuntulani, T. *Top. Curr. Chem.* **2005**, *255*, 163.

(12) (a) Peŕez, J.; Riera, L. *Chem. Commun.* **2008**, 533. (b) Peŕez, J.; Riera, L. *Chem. Soc. Rev.* **2008**, *37*, 2658. (c) Steed, J. W. *Chem. Soc. Rev.* **2009**, *38*, 506.

(13) (a) Beer, P. D.; Kocian, O.; Mortimer, R. J.; Ridgway, C. *J. Chem. Soc., Chem. Commun.* **1991**, 1460. (b) Ward, M. D.; Barigelletti, F. *Coord. Chem. Rev.* **2001**, *216*, 127. (c) Charbonniere, L. J.; Ziessel, R. F.; Sams, C. A.; Harriman, A. *Inorg. Chem.* **2003**, *42*, 3466. (d) Li, M. J.; Chu, B. W. K.; Yam, V. W.-W. *Chem.—Eur. J.* **2006**, *12*, 3528. (e) Davidson, G. J. E.; Loeb, S. J.; Passaniti, P.; Silvi, S.; Credi, A. *Chem.—Eur. J.* **2006**, *12*, 3233. (f) Yam, V. W.-W.; Lee, V. W. M. *J. Chem. Soc., Dalton Trans.* **1997**, 3005. (g) Yam, V. W.-W.; Tang, R. P. L.; Wong, K. M. C.; Lu, X. X.; Cheung, K. K.; Zhu, N. Y. *Chem.—Eur. J.* **2002**, *8*, 4066. (h) Yam, V. W.-W.; Lu, X. X.; Ko, C. C. *Angew. Chem., Int. Ed.* **2003**, *42*, 3385.

(14) (a) Das, S.; Saha, D.; Karmakar, S.; Baitalik, S. *J. Phys. Chem. A.* **2012**, *116*, 5216. (b) Das, S.; Saha, D.; Mardanya, S.; Baitalik, S. *Dalton Trans.* **2012**, *41*, 12296.

(15) (a) Costes, J.-P.; Serra, J.-F.; Dahan, F.; Laurent, J.-P. *Inorg. Chem.* **1986**, *25*, 2790. (b) Costes, J.-P.; Dahan, F.; Laurent, J.-P. *Inorg. Chem.* **1991**, *30*, 1887. (c) Costes, J.-P.; Fernandezcarcia, M. I. *Inorg. Chim. Acta* **1990**, *173*, 241. (d) Fellah, F. Z. C.; Costes, J.-P.; Duhayon, C.; Daran, J.-C.; Tuchagues, J.-P. *Polyhedron* **2010**, *29*, 2111.

(16) (a) Hage, R.; Dijkhuis, A. H. J.; Haasnoot, J. G.; Prins, R.; Reedijk, J.; Buchanan, B. E.; Vos, J. G. *Inorg. Chem.* **1988**, *27*, 2185. (b) Hage, R.; Haasnoot, J. G.; Nieuwenhuis, H. A.; Reedijk, J.; De Ridder, D. J. A.; Vos, J. G. *J. Am. Chem. Soc.* **1990**, *112*, 9245. (c) Serroni, S.; Campagna, S.; Denti, G.; Keyes, T. E.; Vos, J. G. *Inorg. Chem.* **1996**, *35*, 4513.

(17) (a) Haga, M. *Inorg. Chim. Acta* **1980**, *45*, L183. (b) Bond, A. M.; Haga, M. *Inorg. Chem.* **1986**, *25*, 4507. (c) Haga, M.; Bond, A. L. *Inorg. Chem.* **1991**, *30*, 475. (d) Haga, M.; Ali, M. M.; Arakawa, R. *Angew. Chem., Int. Ed. Engl.* **1996**, *35*, 76.

(18) (a) Xie, L.-X.; Hou, X.-W.; Fan, Y.-T.; Hou, H.-W. *Cryst. Growth Des.* **2012**, *12*, 1282. (b) Gu, Z.-G.; Liu, Y.-T.; Hong, X.-J.; Zhan, Q.-G.; Zheng, Z.-P.; Zheng, S.-R.; Li, W.-S.; Hu, S.-J.; Cai, Y.-P. *Cryst. Growth Des.* **2012**, *12*, 2178. (c) Zhang, F.; Li, Z.; Ge, T.; Yao, H.; Li, G.; Lu, H.; Zhu, Y. *Inorg. Chem.* **2010**, *49*, 3776. (d) Wang, Y.-L.; Yuan, D.-Q.; Bi, W.-H.; Li, X.; Li, X.-J.; Li, F.; Cao, R. *Cryst. Growth Des.* **2005**, *5*, 1849. (e) Lu, W.-G.; Jiang, L.; Feng, X.-L.; Lu, T.-B. *Cryst. Growth Des.* **2006**, *6*, 564. (f) Cai, S.-L.; Zheng, S.-R.; Wen, Z.-Z.; Fan, J.; Zhang, W.-G. *Cryst. Growth Des.* **2012**, *12*, 2355. (g) Cai, S.-L.; Zheng, S.-R.; Wen, Z.-Z.; Fan, J.; Zhang, W.-G. *Cryst. Growth Des.* **2012**, *12*, 3575. (h) Wang, C.-F.; Dai, G.-L.; Jin, Z.-N. *Inorg. Chim. Acta* **2013**, *394*, 255. (i) Cai, S.-L.; Zheng, S.-R.; Wen, Z.-Z.; Fan, J.; Wang, N.; Zhang, W.-G. *Cryst. Growth Des.* **2012**, *12*, 4441. (j) Jayaramulu, K.; Reddy, S. K.; Hazra, A.; Balasubramanian, S.; Maji, T. K. *Inorg. Chem.* **2012**, *51*, 7103. (k) Wang, K.-W.; Chen, J.-L.; Cheng, Y.-M.; Chung, M.-W.; Hsieh, C.-C.; Lee, G.-H.; Chou, P.-T.; Chen, K.; Chi, Y. *Inorg. Chem.* **2010**, *49*, 1372. (l) Lu, W.-G.; Jiang, L.; Feng, X.-L.; Lu, T.-B. *Cryst. Growth Des.* **2008**, *8*, 986. (m) Lu, W.-G.; Zhong, D.-C.; Jiang, L.; Lu, T.-B. *Cryst. Growth Des.* **2012**, *12*, 3675. (n) Lu, W.-G.; Su, C.-Y.; Lu, T.-B.; Jiang, L.; Chen, J.-M. *J. Am. Chem. Soc.* **2006**, *128*, 34. (o) Gu, Z.-G.; Cai, Y.-P.; Fang, H.-C.; Zhou, Z.-Y.; Thallapally, P. K.; Tian, J.; Liu, J.; Exarhos, G. J. *Chem. Commun.* **2010**, *46*, 5373. (p) Zheng, S.-R.; Cai, S.-L.; Pan, M.; Fan, J.; Xiao, T.-T.; Zhang, W.-G. *CrystEngComm* **2011**, *13*, 883.

(19) Sullivan, B. P.; Meyer, T. J. *Inorg. Chem.* **1978**, *17*, 3334.

(20) Lay, P. A.; Sargeson, A. M.; Taube, H. *Inorg. Synth.* **1986**, *24*, 291.

(21) *SAINT*, version 6.02 and *SADABS*, version 2.03; Bruker AXS Inc.: Madison, WI, U.S.A., 2002.

(22) Sheldrick, G. M. *SHELXL-97: Program for the Refinement of Crystal Structures*; University of Göttingen: Göttingen, Germany, 1997.

(23) *SHELXTL*, version 6.10; Bruker AXS Inc.: Madison, WI, U.S.A., 2002.

(24) PLATON, see: Spek, A. L. *J. Appl. Crystallogr.* **2003**, *36*, 7−13.

(25) Frisch, M. J.; Trucks, G. W.; Schlegel, H. B.; Scuseria, G. E.; Robb, M. A.; Cheeseman, J. R.; Scalmani, G.; Barone, V.; Mennucci, B.; Petersson, G. A.; Nakatsuji, H.; Caricato, M.; Li, X.; Hratchian, H. P.; Izmaylov, A. F.; Bloino, J.; Zheng, G.; Sonnenberg, J. L.; Hada, M.; Ehara, M.; Toyota, K.; Fukuda, R.; Hasegawa, J.; Ishida, M.; Nakajima, T.; Honda, Y.; Kitao, O.; Nakai, H.; Vreven, T.; Montgomery, J. A., Jr.; Peralta, J. E.; Ogliaro, F.; Bearpark, M.; Heyd, J. J.; Brothers, E.; Kudin, K. N.; Staroverov, V. N.; Kobayashi, R.; Normand, J.; Raghavachari, K.; Rendell, A.; Burant, J. C.; Iyengar, S. S.; Tomasi, J.; Cossi, M.; Rega, N.; Millam, J. M.; Klene, M.; Knox, J. E.; Cross, J. B.; Bakken, V.; Adamo, C.; Jaramillo, J.; Gomperts, R.; Stratmann, R. E.; Yazyev, O.; Austin, A. J.; Cammi, R.; Pomelli, C.; Ochterski, J. W.; Martin, R. L.; Morokuma, K.; Zakrzewski, V. G.; Voth, G. A.; Salvador, P.; Dannenberg, J. J.; Dapprich, S.; Daniels, A. D.; Farkas, Ö.; Foresman, J. B.; Ortiz, J. V.; Cioslowski, J.; Fox, D. J. *Gaussian 09*, revision A.02; Gaussian Inc.: Wallingford, CT, 2009.

(26) Becke, A. D. *J. Chem. Phys.* **1993**, *98*, 5648.

(27) Lee, C. T.; Yang, W. T.; Parr, R. G. *Phys. Rev. B* **1988**, *37*, 785.

(28) Hay, P. J.; Wadt, W. R. *J. Chem. Phys.* **1985**, *82*, 299.

(29) (a) Andrae, D.; Haeussermann, U.; Dolg, M.; Stoll, H.; Preuss, H. *Theor. Chim. Acta.* **1990**, *77*, 123. (b) Fuentealba, P.; Preuss, H.; Stoll, H.; Szentpaly, L. V. *Chem. Phys. Lett.* **1989**, *89*, 418.

(30) Casida, M. Time Dependent Density Functional Response Theory for Molecules. In *Recent Advances in Density Functional Methods*; Chong, D. P., Ed.; World Scientific: Singapore, 1995; Vol. *1*, p 155.

(31) Matsuzawa, N. N.; Ishitani, A. *J. Phys. Chem. A* **2001**, *105*, 4953.

(32) Bauernschmitt, R.; Ahlrichs, R. *Chem. Phys. Lett.* **1996**, *256*, 454.

(33) Stratmann, R. E.; Scuseria, G. E.; Frisch, M. J. *J. Chem. Phys.* **1998**, *109*, 8218.

(34) Casida, M. E.; Jamorski, C.; Casida, K. C.; Salahub, D. R. *J. Chem. Phys.* **1998**, *108*, 4439.

(35) Walters, V. A.; Hadad, C. M.; Thiel, Y.; Colson, S. D.; Wiberg, K. B.; Johnson, P. M.; Foresman, J. B. *J. Am. Chem. Soc.* **1991**, *113*, 4782.

(36) Cossi, M.; Scalmani, G.; Rega, N.; Barone, V. *J. Chem. Phys.* **2002**, *117*, 43.

(37) Tomasi, J.; Mennucci, B.; Cammi, R. *Chem. Rev.* **2005**, *105*, 2999.

(38) (a) Barone, V.; Cossi, M. *J. Phys. Chem. A* **1998**, *102*, 1995. (b) Cossi, M.; Barone, V. *J. Chem. Phys.* **2001**, *115*, 4708. (c) Cossi, M.; Rega, N.; Scalmani, G.; Barone, V. *J. Comput. Chem.* **2003**, *24*, 669.

(39) Caricato, M.; Mennucci, B.; Tomasi, J.; Ingrosso, F.; Cammi, R.; Corni, S.; Scalmani, G. *J. Chem. Phys.* **2006**, *124*, 124520.

(40) Mennucci, B.; Cappelli, C.; Guido, C. A.; Cammi, R.; Tomasi, J. *J. Phys. Chem. A* **2009**, *113*, 3009.

(41) O'Boyle, N. M.; Tenderholt, A. L.; Langner, K. M. *J. Comput. Chem.* **2008**, *29*, 839.

(42) Dennington, R.; Keith, T.; Millam, J. *GaussView*, version 5; Semichem Inc.: Shawnee Mission, KS, 2009.

(43) ORTEP-32 for Windows: Farrugia, L. J. *J. Appl. Crystallogr.* **1997**, *30*, 565.

(44) Vlcek, A.; Zalis, S. *Coord. Chem. Rev.* **2007**, *251*, 258.

(45) Daul, C.; Baerends, E. J.; Vernooijs, P. *Inorg. Chem.* **1994**, *33*, 3538.

(46) (a) Robson, K. C. D.; Koivisto, B. D.; Yella, A.; Sporinova, B.; Nazeeruddin, M. K.; Baumgartner, T.; Grätzel, M.; Berlinguette, C. P. *Inorg. Chem.* **2011**, *50*, 5494−5508. (b) Nazeeruddin, M. K.; De Angelis, F.; Fantacci, S.; Selloni, A.; Viscardi, G.; Liska, P.; Ito, S.; Bessho, T.; Grätzel, M. *J. Am. Chem. Soc.* **2005**, *127*, 16835−16847. (c) De Angelis, F.; Fantacci, S.; Mosconi, E.; Nazeeruddin, M. K.; Grätzel, M. *J. Phys. Chem. C* **2011**, *115*, 8825−8831. (d) De Angelis, F.; Fantacci, S.; Selloni, A.; Nazeeruddin, M. K.; Grätzel, M. *J. Am. Chem. Soc.* **2007**, *129*, 14156−14157.

(47) (a) Wächtler, M.; Kupfer, S.; Guthmuller, J.; Pop, J.; González, L.; Dietzek, B. *J. Phys. Chem. C* **2011**, *115*, 24004. (b) Kupfer, S.; Guthmuller, J.; Wächtler, M.; Losse, S.; Rau, S.; Dietzek, B.; Popp, J.; Gonzalez, L. *Phys. Chem. Chem. Phys.* **2011**, *13*, 15580.

(48) (a) Fantacci, S.; De Angelis, F.; Selloni, A. *J. Am. Chem. Soc.* **2003**, *125*, 4381. (b) De Angelis, F.; Fantacci, S.; Gebauer, R. *J. Phys. Chem. Lett.* **2011**, *2*, 813.

(49) (a) Chou, C. C.; Wu, K. L.; Chi, Y.; Hu, W. P.; Yu, S. J.; Lee, G. H.; Lin, C. L.; Chou, P. T. *Angew. Chem., Int. Ed.* **2011**, *50*, 2054. (b) Lee, T.-C.; Hung, J.-Y.; Chi, Y.; Cheng, Y.-M.; Lee, G.-H.; Chou, P.-T.; Chen, C.-C.; Chang, C.-H.; Wu, C.-C. *Adv. Funct. Mater.* **2009**, *19*, 2639.

(50) (a) Rekhis, M.; Labat, F.; Ouamerali, O.; Ciofini, I.; Adamo, C. *J. Phys. Chem. A* **2007**, *111*, 13106. (b) Guillemoles, J.-F.; Barone, V.; Joubert, L.; Adamo, C. *J. Phys. Chem. A* **2002**, *106*, 11354. (c) Ciofini, I.; Lainé, P. P.; Bedioui, F.; Adamo, C. *J. Am. Chem. Soc.* **2004**, *126*, 10763.

(51) (a) Wang, J.; Bai, F.-Q.; Xia, B.-H.; Sun, L.; Zhang, H.-X. *J. Phys. Chem. A* **2011**, *115*, 1985−1991. (b) Li, M. X.; Zhou, X.; Xia, B. H.; Zhang, H.-X.; Pan, Q. J.; Liu, T.; Fu, H. G.; Sun, C. C. *Inorg. Chem.* **2008**, *47*, 2312−2324.

(52) Klein, S.; Dougherty, W. G.; Kassel, W. S.; Dudley, T. J.; Paul, J. J. *Inorg. Chem.* **2011**, *50*, 2754.

(53) Su, J.; Shi, L.; Sun, X.; Guan, W.; Wu, Z. *Dalton Trans.* **2011**, *40*, 11131.

(54) (a) Monat, J. E.; Rodriguez, J. H.; McCusker, J. K. *J. Phys. Chem. A* **2002**, *106*, 7399. (b) McCusker, J. K. *Acc. Chem. Res.* **2003**, *36*, 876. (c) Damrauer, N. H.; Boussie, T. R.; Devenney, M.; McCusker, J. K. *J. Am. Chem. Soc.* **1997**, *119*, 8253. (d) McCusker, C. E.; McCusker, J. K. *Inorg. Chem.* **2011**, *50*, 1656.

(55) (a) Garner, R. N.; Joyce, L. E.; Turro, C. *Inorg. Chem.* **2011**, *50*, 4384. (b) Sun, Y.; Ojaimi, M. E.; Hammitt, R.; Thummel, R. P.; Turro, C. *J. Phys. Chem. B* **2010**, *114*, 14664. (c) Sun, Y.; Liu, Y.; Turro, C. *J. Am. Chem. Soc.* **2010**, *132*, 5594. (d) Sun, Y.; Collins, S. N.; Joyce, L. E.; Turro, C. *Inorg. Chem.* **2010**, *49*, 4257.

(56) Wadman, S. H.; Kroon, J. M.; Bakker, K.; Havenith, R. W. A.; van Klink, G. P. M.; van Koten, G. *Organometallics* **2010**, *29*, 1569.

(57) (a) Coe, B. J.; Thompson, D. W.; Culbertson, C. T.; Schoonover, J. R.; Meyer, T. J. *Inorg. Chem.* **1995**, *34*, 3385. (b) Kober, E. M.; Meyer, T. J. *Inorg. Chem.* **1982**, *21*, 3967.

(58) (a) Liu, Y.; Hammitt, R.; Lutterman, D. A.; Thummel, R. P.; Turro, C. *Inorg. Chem.* **2007**, *46*, 6011. (b) Liu, Y.; Hammitt, R.; Lutterman, D. A.; Joyce, L. E.; Thummel, R. P.; Turro, C. *Inorg. Chem.* **2009**, *48*, 375.

(59) Robin, M. B.; Day, P. *Adv. Inorg. Chem. Radiochem.* **1967**, *10*, 247.

(60) Crutchley, R. J. *Adv. Inorg. Chem.* **1994**, *41*, 273.

(61) Wilcox, C. S. *Frontiers in Supramolecular Chemistry and Photochemistry*; Schneider, H.-J., Dürr, H., Eds.; VCH: Weinheim, Germany, 1991; pp 123−143.

(62) Dobrawa, R.; Lysetska, M.; Ballester, P.; Grüne, M.; Würthner, F. *Macromolecules* **2005**, *38*, 1315.

(63) Montalti, M.; Wadhwa, S.; Kim, W. Y.; Kipp, R. A.; Schmehl, R. H. *Inorg. Chem.* **2000**, *39*, 76.

(64) (a) Balzani, V.; Ballardini, R.; Gandolfi, M. T.; Prodi, L. In *Frontiers in Supramolecular Chemistry and Photochemistry*; Schneider, H.-J., Dürr, H., Eds.; VCH: Weinheim, Germany, 1991; pp 371. (b) Balzani, V.; Scandola, F. In *Photoinduced electron transfer. Part D: Photoinduced electron transfer reactions. Inorganic substrates and applications*; Fox, M. A., Chanon, M., Eds.; Elsevier: New York, 1988; p 148. (c) Balzani, V.; Sabbatini, N.; Scandola, F. *Chem. Rev.* **1986**, *86*, 319.